RSC Advances

PAPER

View Article Online
View Journal | View Issue

Cite this: *RSC Adv.*, 2024, **14**, 17413

Design of a new palladium(II) halide complex as a bio-active material: synthesis, physico-chemical studies, DFT-computations and evaluation of anti-inflammatory, antioxidant and anti-gastric damage activities†

Sarra Bougossa,[a] Noureddine Mhadhbi,[ab] Ali Ben Ahmed,[c] Mohamed Hamdi,*[d] Kais Elghniji,[e] Jeanneau Erwann,[f] Khaled Hamden,[g] Abderrazek Oueslati[h] and Houcine Naïli*[a]

Received 22nd April 2024
Accepted 18th May 2024

DOI: 10.1039/d4ra02984d

rsc.li/rsc-advances

Colorless single crystals of the zero-dimensional hybrid compound, $(C_6H_{10}N_2)_2[PdCl_6]\cdot 2H_2O$ were acquired through the slow evaporation technique. The crystal structure was explored using SC-XRD, which demonstrates that the material crystallizes in the centrosymmetric space group $P\bar{1}$ of the triclinic system. The density functional theory method at the B3LYP/Lan2mb basis set level was employed to establish the optimized geometry and vibrational frequencies of the title compound. An acceptable correspondence was observed between the results obtained through calculation and the experimental data, including the structure, and IR spectra. The optical characteristics revealed a direct band gap energy of 2.35 eV, validating the semiconductor characteristics of this new material. The results suggest strong agreement with the experimental data and validate the involvement of metal orbitals in defining the HOMO–LUMO boundary. Simultaneous TGA-DTA shows that this material remains solid up to 210 °C. Beyond these temperatures, a gradual decomposition process occurs, extending up to 440 °C and unfolding in several steps. This process entails the liberation of diverse compounds, encompassing organic molecules, and the evaporation of chlorine ions, ultimately leading to the formation of palladium oxide (PdO) as the final product. When given to rats with gastric ulcers at a dose of 100 mg kg^{-1}, these compounds inhibit the key enzyme responsible for neutrophil infiltration as myeloperoxidase (MPO) by 38.7%. The compound also alleviates cellular damage induced by free radicals, demonstrated by a notable 48.3% decrease in thiobarbituric acid reactive substance rates (TBARS) compared to untreated rats. Additionally, these compounds bring about a substantial 30.6% reduction in the surface area of ulcers.

1 Introduction

Hybrid systems stand out due to their compelling characteristics, which stem from the amalgamation of exceptional traits found in both organic and inorganic molecules. This unique blend has sparked considerable scientific interest, making hybrid systems a prominent area of research that captivates researchers worldwide. Taking applications one step further, hybrid materials cover a wide range of fields, including sensors,[1],[2] magnetic,[3–5] optical (nonlinear optics),[6,7] electroluminescence,[8] ionic,[9] and medical[9–11] fields. In the literature, many organic molecules are utilized as templates for metal halides. However, several studies have identified 3-(aminomethyl)pyridine (3-Amp) as a liquid with an evident yellowish color, which serves as a crucial amine in the pharmaceutical sector.[12,13]

The palladium has been combined with 3-AMP to produce a new hybrid compound that merges inorganic and organic elements. Typically, the inorganic lattice is formed by layers of

---

[a] Laboratory of Solid State (LR11ES51), Faculty of Sciences, University of Sfax, BP 1171, 3000 Sfax, Tunisia. E-mail: houcine_naili@yahoo.com

[b] University of Monastir, Preparatory Institute for Engineering Studies of Monastir, 5019 Monastir, Tunisia

[c] Laboratory of Applied Physics, University of Sfax, Faculty of Sciences, Sfax, Tunisia

[d] Department of Chemistry, College of Siences and Arts Turaif, Northern Border University, Arar, Saudi Arabia. E-mail: Mohamed.Hamdi@nbu.edu.sa

[e] Laboratory of Materials applications in Environment, Water and Energy LAMEEE (LAM3E), Faculty of Sciences of Gafsa, University of Gafsa, Sidi Ahmed Zarroug University campus, 2112 Gafsa, Tunisia

[f] Centre de Diffractométrie Henri Longchambon, Université Claude Bernard Lyon 1, 5 Rue de La Doua, 69100 Villeurbanne, France

[g] Laboratory of Bioresources: Integrative Biology and Exploiting, Higher Institute of Biotechnology of Monastir, University of Monastir, Tunisia

[h] Laboratory of Spectroscopic Characterization and Optical Materials, Faculty of Sciences, University of Sfax, B. P. 1171, 3000 Sfax, Tunisia

† Electronic supplementary information (ESI) available. CCDC 2331639. For ESI and crystallographic data in CIF or other electronic format see DOI: https://doi.org/10.1039/d4ra02984d

octahedra (MX_6) or tetrahedra (MX_4) along with organic cations, which can be linear or aromatic. The interaction between these components results in the creation of a supramolecular network characterized as a pseudo-zero-dimensional structure, largely facilitated by noncovalent interactions. These complexes are generally stabilized by hydrogen bonds and low-energy van der Waals forces. In this study, we present the crystal structure, as well as analyses including Infrared spectroscopy (IR), Raman spectroscopy, optical absorption, and photoluminescence measurements. Additionally, we conduct Hirshfeld surface (HS) analysis, cyclic voltammetry, and thermal analysis of the compound. Furthermore, we compare our experimental findings with density functional theory (DFT) calculations.

Inflammation has a major role in pathological complications such cancer, metabolic, cardiovascular, rheumatic, and arthritic conditions. Various analgesic and anti-inflammatory drugs could be used therapeutically to treat the diseases linked to inflammation.[14–16] Corticosteroids and non-steroidal anti-inflammatory medicines (NSAIDs) are currently being used clinically to treat inflammatory illnesses. However, long-term usage of corticosteroids is linked to osteoporosis, weight gain, and an immunosuppressive effect; chronic high-dose NSAID intakes are often linked to GIT toxicity.[17] Therefore, finding and creating alternative anti-inflammatory drugs from other sources that are more effective and tolerable at this point is difficult for researchers. Numerous anti-inflammatory and analgesic effects of the compounds containing palladium thiocarbamate in their structure have been outlined.[14–18] According to reports, the dithiocarbamates show promise in preventing nitrative stress, cytokine production, and oxidative stress.[19] In light of the discovery mentioned above, we therefore decided to investigate the newly produced new palladium(II) halide complex for possible therapeutic effects, including anti-inflammatory and antioxidant properties in gastric tissues.

2 Experimental details

2.1. Synthesis of the crystal sample

The organic–inorganic compound was prepared by mixing, in stoichiometric proportions [2 : 1], a solution of 3-(aminomethyl) pyridine ($C_6H_8N_2$) (2 mmol) and a solution of palladium chloride [$PdCl_2$] (1 mmol) previously dissolved in 10 ml of distilled water with a small amount of hydrochloric acid present. The blend was stirred magnetically for 10 minutes at room temperature, leading to the creation of homogeneous solutions. The reaction sequence for the synthesis is shown in the following schema (Scheme 1).

The resulting block and colorless crystals of $(C_6H_{10}N_2)[PdCl_6]\cdot 2H_2O$ were acquired following several days of gradual evaporation of the mixture at room temperature. The crystals underwent washing with ether, meticulous filtration, and air-drying for a day before being gathered for subsequent physical and chemical analyses.

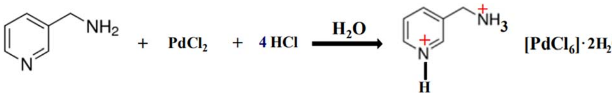

Scheme 1 Synthesis of complex $(C_6H_{10}N_2)$ $[PdCl_6]\cdot 2H_2O$.

2.2. X-ray data collection

A solitary colorless crystal block of specified dimensions of 0.35 × 0.34 × 0.16 mm^3 was carefully selected for data collection using Xcalibur, Atlas, Gemini ultra diffractometer employing fine-focus sealed X-ray tube, enhance (Mo) X-ray source, to gather all reflections at room temperature. The angular range between $3.4° < \theta < 29.3°$ gives the following values as bounds of the Miller indices (h, k, l) of the measured reflections $h = -10 \rightarrow 10$, $k = -10 \rightarrow 10$, $l = -13 \rightarrow 13$. 13 853 reflections were recorded, of which 2682 independent reflections, 2179 having intensity $I > 2\sigma(I)$. The different structural parameters: atomic positions, isotropic (U_{iso}) or anisotropic (U_{aniso}) displacement parameters, and statistical occupancy of crystallographic sites, the refinement of these parameters utilized the least squares method applied to the square of the modulus of the structure factors $|F^2|$. The structure was solved with SHELXS-97 (ref. 20) and refined using SHELXL-97(ref. 21) all of which were used with the WINGX software.[22] The hydrogen atom positions of the protonated amine $[C_6H_{10}N_2]^{2+}$ were fixed geometrically using the HFIX option included in SHELXL-97.[21] The molecular structure drawing was constructed using Diamond 3.2.[23] The final values of the unweighted and weighted reliability factors are $R_1 = 0.056$ and $wR_2 = 0.159$ respectively. The recording conditions and refinement results are summarized in Table 1 and 2 summarizes the atomic coordinates, equivalent thermal stirring factors ($U_{\text{eq.}}$) of the compound, and the equivalent thermal stirring factors and anisotropy are given in Table 3.

2.3. Spectroscopic measurements

Spectroscopic measurements were employed to identify functional groups and gain additional insights into the molecular structure of the synthesized compound. FT-IR is regarded as one of the most powerful techniques utilized for identifying the vibrational frequencies of the atomic bonds comprising the material. The infrared absorption spectrum of the compound in question was recorded using a PerkinElmer BX FT-IR spectrometer, covering the range of 400–4000 cm^{-1} at room temperature.

The optical absorption spectrum of the films was obtained at room temperature utilizing a standard UV-visible absorption spectrometer, spanning wavelengths from 190 nm to 800 nm. Meanwhile, the photoluminescence spectrum was recorded employing a Dilor XY configuration, with an excitation wavelength of 586 nm, covering the range from 200 to 500 nm using a solid sample at room temperature. The determination of the HOMO–LUMO energy levels and the electrochemical band gaps (E_g) involved considering the oxidation and reduction onset values.

2.4. Electrochemical measurements

Room temperature electrochemical evaluations were performed using a CHI 660B electrochemical analyzer. The setup utilized a standard three-electrode configuration, comprising a glassy carbon electrode as the working electrode, an Ag/AgCl electrode

Table 1 Crystal data and structure refinement parameters for $(C_6H_{10}N_2)_2[PdCl_6]\cdot 2H_2O$

Empirical formula	$C_{12}H_{24}Cl_6PdN_4O_2$
Formula weight (g mol^{-1})	575.45
Temperature (K)	150
Crystal system	Triclinic
Space group	$P\bar{1}$
a (Å)	7.720(8)
b (Å)	7.794(8)
c (Å)	9.597(9)
α (°)	81.799(8)
β (°)	83.134(8)
γ (°)	66.739(10)
V (Å^3)	523.91(10)
Z	1
D_x (mg m^{-3})	1.824
μ (mm^{-1})	1.67
Crystal size (mm^3)	0.35 × 0.34 × 0.16
Crystal color/shape	Block, colourless
hkl range	$-10 \le h \le 10$; $-10 \le k \le 10$; $-13 \le l \le 13$
θ (°)	2.9–29.5
Diffractometer	Xcalibur, Atlas, Gemini ultra diffractometer
$R_1{}^a$, w$R_2{}^b$ [$I > 2(I)$]	0.056, 0.159
GooF on F^2	1.19
$\Delta\rho_{\max}$ (e Å^{-3})	1.71
$\Delta\rho_{\min}$ (e Å^{-3})	−1.69

[a] $R_1 = \sum|F_o| - |F_c|/\sum|F_o|$. [b] $wR_2 = [\sum w(F_o{}^2 - F_c{}^2)^2/\sum w(F_o{}^2)^2]^{1/2}$.

as the reference electrode, and a platinum wire as the counter electrode.

2.5. Thermal analysis

The thermal stability of the crystal under investigation was examined through thermogravimetric analysis (TGA) combined with differential thermal analysis (DTA) using a TGA/DTA instrument named “SETSYS Evolution” with a Pt crucible and Al_2O_3 as the reference material. The analysis was conducted under airflow conditions with a heating rate of 5 °C min^{-1}, starting from room temperature and reaching up to 550 °C. The sample initially weighed 19 mg, and thermograms were collected throughout the process.

2.6. Computational studies

In this study, the Gaussian 09W program package[24] was utilized with DFT/B3LYP/Lanl2mb basis set level for calculating the properties of the title molecule. Furthermore, a cluster was constructed from extracted single crystal X-ray data containing one $[PdCl_6]$ anion, one [3-AMP]$^{2+}$ cation and one isolated molecule of water connected by N–H⋯O hydrogen bonds (Fig. 1b). Subsequently, the optimized geometry was utilized as an input file for calculating the infrared spectrum, UV-visible absorption, HOMO–LUMO and second hyperpolarizability. Corrective measures were employed to obtain the harmonic vibrational frequencies, ensuring a robust correlation between the experimental and calculated outcomes.

The quartet ground state geometry optimization of the complex was conducted using the default convergence criteria, without imposing any constraints on the geometry.[25] Frequency analysis of the optimized geometry, performed at the same level of theory, confirmed the structure as a true local minimum, exhibiting no imaginary frequencies. To correct for systematic errors arising from basis set incompleteness, neglect of electron correlation, and vibrational anharmonicity, an empirical scaling factor of 0.961 was applied.[26] Electronic properties were evaluated using a time-dependent DFT (TD-DFT) approach[27] at the same level of theory. The calculated results, including vertical excitation energies, oscillator strength (f), and frequencies, were compared with experimentally measured wavelengths. The simulated absorption spectrum, employing the GAUSSIAN 09, was generated using the GAUSSUM version 2.2 software package,[28] while the GaussView 05 program[29] was utilized to visualize the iso-density plots of frontier orbitals.

2.7. Conductivity evaluations

Electrical measurements were conducted on a pellet measuring 8 mm in diameter and 1 mm in thickness. Conducting silver paint was applied to the opposing sides of the pellet to establish a robust electrical connection. AC impedance spectroscopy was used to investigate the sample's transport characteristics using a 1260 Solartron Impedance Analyzer in vacuum, working over a frequency range of 10^2 to 10^7 Hz and at temperatures ranging from 313 to 358 K with an AC voltage of 0.5 V.

2.8. Animals

For this investigation, male mice weighing roughly 30 g were used. The rats had access to water and were fed pellets. The setting in which the animals were kept was regulated. Rat experiments were conducted in accordance with international care and use Laboratory Animals (code: 86/609/EEC) criteria at Monastir University. EtOH was given to the rats at a dose of

Table 2 Experimental and optimized molecular geometric parameters of $(C_6H_{10}N_2)_2[PdCl_6]\cdot 2H_2O$

Geometric parameters	Calculated	XRD data	Δ (%)
Bond lengths (Å) calc.			
Pd1–Cl1[a]	2.642	2.7106(14)	2.5
Pd1–Cl1	2.573	2.7106(14)	5.05
Pd1–Cl2	2.570	2.6130(15)	1.64
Pd1–Cl2[a]	2.447	2.6130(15)	6.35
Pd1–Cl3[a]	2.465	2.6363(14)	6.49
Pd1–Cl3	2.470	2.6364(14)	6.31
N1–C1	1.448	1.347(10)	6.97
N1–C5	1.405	1.338(9)	4.76
N2–C6	1.560	1.488(8)	4.61
C1–C2	1.405	1.357(11)	3.41
C2–C3	1.364	1.373(10)	0.65
C3–C4	1.463	1.396(9)	4.57
C4–C5	1.378	1.377(9)	0.07
C4–C6	1.526	1.512(9)	0.91
Bond angles (°)			
Cl1i–Pd1–Cl1	178.22	180.0	0.98
Cl2–Pd1–Cl1	92.12	91.98(5)	0.15
Cl2–Pd1–Cl1[a]	90.06	88.02(5)	2.26
Cl2i–Pd1–Cl1[a]	90.19	91.98(5)	1.94
Cl2i–Pd1–Cl1	89.95	88.02(5)	2.14
Cl2–Pd1–Cl2[a]	178.66	180.0	0.74
Cl2–Pd1–Cl3[a]	89.95	89.94(5)	0.01
Cl2–Pd1–Cl3	89.21	90.06(5)	0.94
Cl3i–Pd1–Cl1	88.32	87.66(4)	0.74
Cl3–Pd1–Cl1[a]	87.75	87.66(4)	0.10
Cl3–Pd1–Cl1	93.57	92.34(4)	1.31
Cl3–Pd1–Cl3[a]	176.36	180.0	2.02
C5–N1–C1	122.35	122.4(6)	0.04
N1–C1–C2	117.02	119.5(6)	2.07
C1–C2–C3	120.14	120.3(7)	0.13
C2–C3–C4	121.85	119.1(6)	2.25
C3–C4–C6	121.35	121.4(6)	0.04
C5–C4–C3	117.83	119.0(6)	0.98
C5–C4–C6	120.75	119.6(6)	0.95
N1–C5–C4	120.64	119.5(6)	0.94
N2–C6–C4	109.42	111.2(5)	1.60

[a] Symmetry code: $-x + 1, -y + 1, -z$.

Table 3 Intermolecular hydrogen bonds (Å, °) in $(C_6H_{10}N_2)_2[PdCl_6]\cdot 2H_2O$

D–H···A	D–H	H···A	D···A	D–H···A
O1–H1B···Cl1	0.85	2.47	3.210(5)	146
O1–H1C···Cl3	0.85	2.33	3.149(5)	161
N1–H1···O1[a]	0.86	1.87	2.706(8)	163
N2–H2A···Cl1[b]	0.89	2.36	3.240(5)	172
N2–H2B···Cl1[c]	0.89	2.36	3.199(6)	158
N2–H2C···Cl2[d]	0.89	2.62	3.259(6)	129
N2–H2C···Cl2[e]	0.89	2.58	3.238(6)	131
C1–H1A···Cl2[f]	0.93	2.69	3.588(7)	164
C2–H2···Cl1[g]	0.93	2.73	3.571(7)	152
C5–H5···Cl3[e]	0.93	2.63	3.424(7)	143
C6–H6A···Cl1[e]	0.97	2.89	3.767(7)	151
C6–H6B···Cl2[c]	0.97	2.95	3.770(6)	143
C6–H6B···Cl3[h]	0.97	2.85	3.623(7)	137

[a] Symmetry code: $x + 1, y, z$. [b] Symmetry code: $-x + 1, -y + 1, -z + 1$. [c] Symmetry code: $x, y + 1, z + 1$. [d] Symmetry code: $x, y, z + 1$. [e] Symmetry code: $-x + 2, -y + 1, -z + 1$. [f] Symmetry code: $-x + 2, -y + 1, -z$. [g] Symmetry code: $x, y + 1, z$. [h] Symmetry code: $-x + 1, -y + 2, -z + 1$.

5 mL kg^{-1} in order to cause stomach ulcers.[30,31] After that, 20 mice in total—15 with stomach ulcers and 5 healthy mice—were split up into 4 groups. Rats in the first group, known as the control group, were given a regular diet. Rats with ulcers were divided into two groups, U-3A_{50} and U-3A_{100}, respectively, and given doses of 3*A* of 50 mg and 100 mg kg^{-1}. As the ulcerated group, the fourth group was administered omeprazole at a dosage of 20 mg kg^{-1}. After the rats were sacrificed, their stomachs were quickly taken out, rinsed with distilled water, and reopened. The entire area of the ulcer was then computed utilizing an e-ruler-provided digital calculable distance and an inverted microscope equipped with a digital camera and Image J software. The measurement of gastric juice MPO activity was done using spectrophotometry at 460 nm. At 25 °C, the consumption rate of one micromole of peroxide per minute was established as one unit of myeloperoxidase (MPO) activity.[32] Stomach juice TBARS rates were calculated using the method outlined by Buege and Aust.[33]

3 Results and discussion

3.1. Structure description

The present compound crystallizes in the triclinic system, exhibiting a centrosymmetric space group $P\bar{1}$, with lattice parameters as provided below: $a = 7.720(8)$ Å; $b = 7.794(8)$ Å; $c = 9.597(9)$ Å; $\alpha = 81.799(8)°$; $\beta = 83.134(8)°$; $\gamma = 66.739(10)°$ and $Z = 1$.

The fundamental unit of the investigated material, depicted in Fig. 1a, consists of one inorganic $[PdCl_6]^{2-}$ isolated octahedra anion, two-diprotonated 3-aminomethyl pyridinium cation $(C_6H_{10}N_2)^{2+}$ and one water molecule. This aligns well with the optimized geometry of the title compound model depicted in Fig. 1b. The electrical neutrality of this 0D compound is ensured by the alternating cationic layers formed by two $[C_6H_{10}N_2]^{2+}$ entities and the anionic layers formed by the octahedra $[PdCl_6]^{4-}$ projected in the (*a*, *c*) plane as shown in Fig. 2. The parallel arrangement of organic cations between the planes of two adjacent aromatic rings suggests interactions of the type π···π in this compound. Hydrogen bonds of the C/N–H···Cl and N–H···O type, facilitated by nitrogen atoms, ensure the connection between the mineral anion, the organic cation, and the water molecule. Table 4 provides an overview of the primary characteristics of the bond lengths and bond angles in the title compound. In the organic part of the title compound, either of the two nitrogen atoms (N1 or N2) of the amine becomes protonated. Thus, equalizing the two charges borne by the inorganic component. The C–C distances range from 1.357(11) to 1.512(9) Å, while the N–C distances vary between 1.347(10) and 1.338(9) Å. The angles C–N–C, N–C–C, and C–C–C are in the range of 122.4(6)°, 119.5(6)–111.2(5)° and 119.6(6)–120.3(7)°, respectively.

The C–C distances exhibit a range between 1.357(11) and 1.512(9) Å, while the N–C distances fall within 1.347(10) to 1.338(9) Å. The angles C–N–C, N–C–C, and C–C–C are measured within the ranges of 122.4(6)°, 119.5(6)–111.2(5)°, and 119.6(6)–120.3(7)°, respectively.

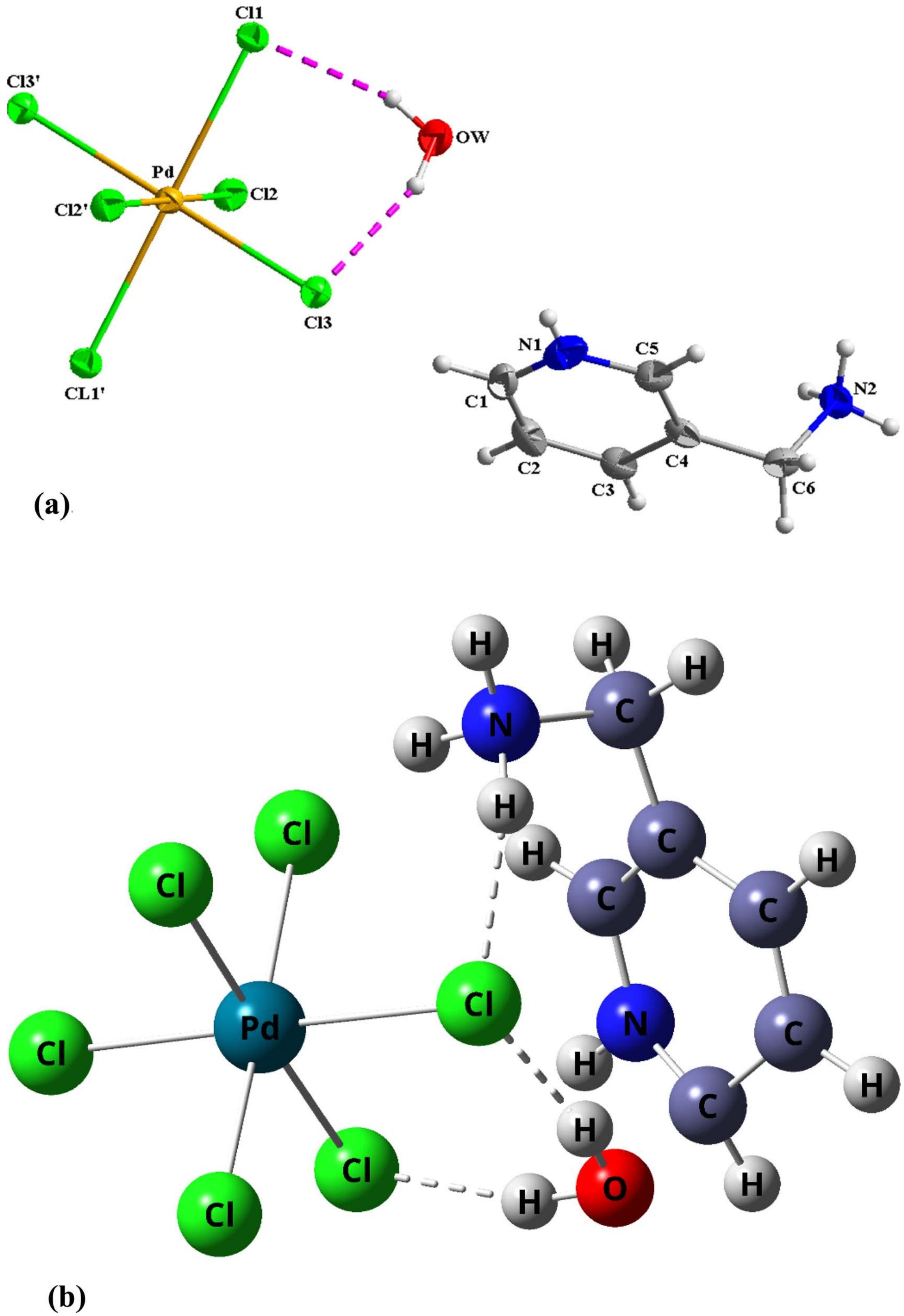

Fig. 1 (a). Representation of the asymmetric unit of $(C_6H_{10}N_2)_2[PdCl_6]\cdot 2H_2O$. (b) Optimized geometry of $(C_6H_{10}N_2)_2[PdCl_6]\cdot 2H_2O$.

The inorganic entities $PdCl_6$ consist of six Cl atoms that surround the Pd^{2+} cation forming an octahedral geometry. The Pd–Cl distances vary between 2.6367(14) and 2.7106(14) Å whereas the Cl–Pd–Cl angles range from 87.66(4) to 180.0°. Table 4 displays the geometrically and experimentally determined parameters. After a thorough examination of these parameters, it becomes evident that the majority of the calculated values are very close to those obtained experimentally. The relative difference for

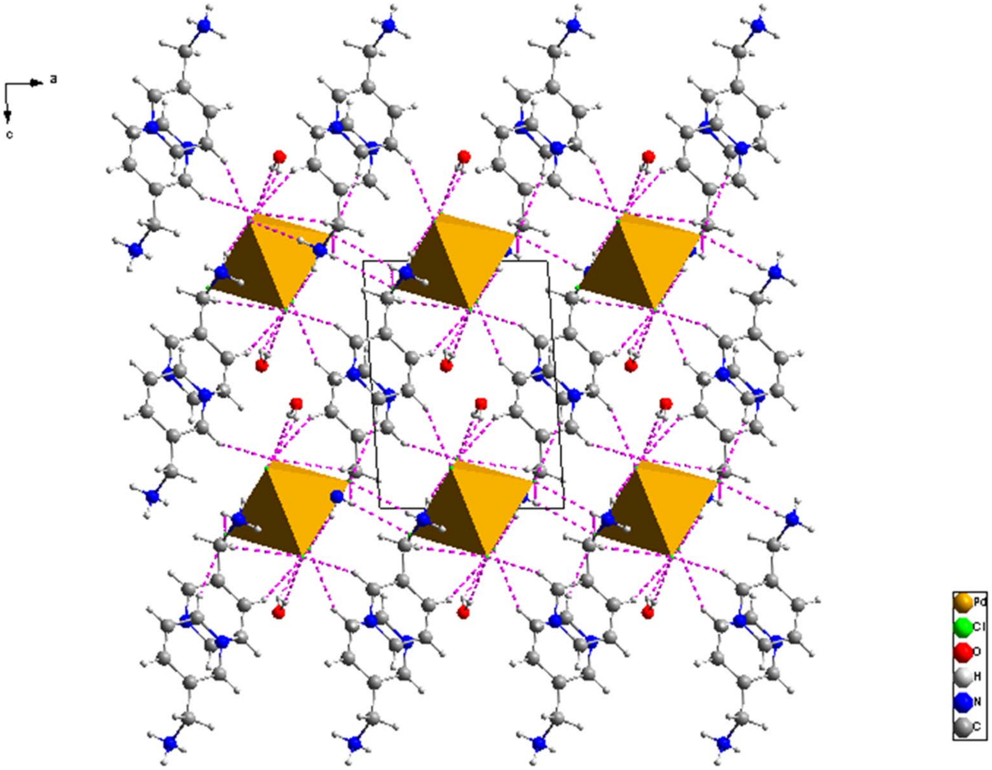

Fig. 2 Projection of the structure of $(C_6H_{10}N_2)_2[PdCl_6]\cdot 2H_2O$ on the (*a*, *c*) plane. The dotted lines indicate the hydrogen bonds.

inorganic structural parameters is approximately 2.8%, while it stays below 1% for organic parameters when comparing experimental and calculated values. Water plays an important role in stabilizing the crystal structure. The resulting H- bonding networks can be characterized by a three-dimensional supramolecular framework. According to Brown,[34] hydrogen bonds of the N–H⋯Cl type existing in this compound are considered weak. As can be seen in Table 5, the organic and mineral components are connected *via* weak hydrogen bonds involving donor–acceptor interactions D⋯A with an upper limit of 3.623(7) Å and a lower limit of 137 Å for D–H⋯A bond angles. This compound under study exhibits three types of hydrogen bonds: the first one, C–H⋯Cl ranging from 2.36 Å to 2.58 Å, while the second one, N–H⋯Cl with distances ranging from 2.69 Å to 2.85 Å, and thirdly N–H⋯O bonds, with H⋯O distance 1.87 Å facilitates the interaction between organic cations and the anionic chains.

3.2. Hirshfeld surfaces analysis

The description of the bonds existing in this material was studied using Hirshfeld surface calculations with CrystalExplorer 3.0 software[35–37] which accepts an input file in CIF format. These interactions were quantified through Hirshfeld surface analysis[38] along with the corresponding two-dimensional fingerprint.[39] The identification of contacts is facilitated through the normalized contact distance (d_{norm}), which considers the distances between the surface and the nearest nucleus inside (d_{i}) and outside (d_{e}) the surface, along with the van der Waals radii of the atom, using the following equation:[40]

$$d_{\text{norm}} = \frac{d_{\text{i}} - r_{\text{i}}^{\text{vdw}}}{r_{\text{i}}^{\text{vdw}}} + \frac{d_{\text{e}} - r_{\text{e}}^{\text{vdw}}}{r_{\text{e}}^{\text{vdw}}} \tag{1}$$

The Hirshfeld surface mapped according to d_{norm} (−0.5087; 1.2448) Å of the compound representing a hybrid architecture based mainly on hydrogen bonds already presented in Table 5 is shown in Fig. 3. The red circular areas are indicators of contacts between the different entities present with shorter contacts ($d_{\text{norm}} < 0$), the blue spots indicate the longest contacts within the structure ($d_{\text{norm}} > 0$), whereas the white spots represent contacts occurring at the sum of the van der Waals separations ($d_{\text{norm}} = 0$). The variation in color intensity indicates the intensity of the interaction. As for Fig. 3b, it displays the occurrence of red and blue triangles on the shape index regions indicating the existence of electrostatic interactions π⋯π between organic entities. In addition, analysis of the 2D fingerprint graphs (Fig. 4) allows us to relate numerical values to d_{norm}-mapped Hirshfeld surfaces and to determine the different contributions relative to the various interactions between the organic molecules and the inorganic part. All these interactions overlap in the total footprint equal to 100% shown in the figure below. The first part of this study highlights the dominance of H⋯Cl/Cl⋯H type hydrogen bonds by a percentage equal to 65%, reflected on the footprint by a wing at the top level. H⋯H interactions have a significant contribution with a percentage of 19.3% as shown in Fig. 4b. Still in the study of the percentage contributions of hydrogen bonds in this structure the presence of H⋯O/O⋯H, H⋯C/C⋯H and, H⋯N/N⋯H interactions

Table 4 Vibrational assignments, experimental and calculated wavenumbers (cm^{-1})

Experience	DFT	Assignments
3424	3686	Asym. O–H (H_2O) stretching
3409	3415	Sym. O–H (H_2O) stretching
3167	3170	C–H (ring) stretching
3064	3076	N–H stretching
3043	3079	Asym. CH_2 stretching
2925	3019	Sym. CH_2 stretching
1729	1739	Ring deformation
1627	1651	H–N–H in plane bending
1602	1625	C–C stretching, in plane bending of H–N–C and H–C–C
1580	1596	C–C–C (ring) deformation
1549	1567	CH_2 deformation
1483	1497	In plane bending of H–C–H
1467	1481	C–H in plane bending
1425	1443	N–H in plane bending
1390	1406	H–C–C–N torsion
1379	1385	N–C stretching
1317	1329	N–C stretching
1246	1261	In plane bending of H–C–N
1225	1239	C–C stretching
1189	1182	C–C–N deformation
1122	1137	CH_2 torsion
1091	1108	Sym. CCN stretching
1070	1087	C–C stretching
1050	1063	H–C–C–H torsion
972	988	C–N elongation
911	924	C–H bending
870	895	C–H (ring) bending
823	859	N–C–C deformation
793	805	H–C–C–H torsion
637	654	Ring deformation
566	578	O–H (H_2O) bending
494	5013	H–C–C–C torsion
406	417	C–C–C–C torsion

Table 5 Global reactivity descriptors

Parameters	Values
E_{HOMO} (eV)	−6.11
E_{LUMO} (eV)	−4.39
$\Delta E_{\mathrm{H-L}}$ (eV)	1.72
I_{P} (eV)	6.11
E_{A} (eV)	4.39
χ (eV)	5.25
μ (eV)	−5.25
η (eV)	1.72
ω (eV)	8.01

account for only 6%, 4.2% and 1.5% of the total contributions, respectively. Calculation of the void in the crystal is illustrated in Fig. 5. The void within the crystalline material was visualized by generating an isosurface (0.002 au) of procrystal density. The resulting void volume is 26.99 Å^3 according to single-crystal XRD analysis, the filled volume is 523.91 Å^3, so the void percentage is 5.15% per unit cell.

3.3. Infrared spectroscopy study

To obtain more information in the description of the crystal structure, focusing on the layers of cationic–anionic functional groups, we have undertaken vibrational spectroscopy using infrared absorption at room temperature. The infrared spectrum of the different bands recorded between 400 and 4000 cm^{-1} of the experimental and the DFT computed superposed are presented in Fig. 6. According to a comparison between the theoretical and experimental modes and frequencies reported in the literature for comparable compounds,[41–43] the assignments of the observed bands are provided in Table 6. Initially, we observe a close match between the experimental and simulated spectra for both infrared and Raman characteristics. Hereafter, we won't provide a comprehensive assignment. Instead, we aim to extract the most pertinent and distinctive information that correlates with structural properties. It's worth mentioning that the regions of high frequencies, specifically 3424 cm^{-1} and 3409 cm^{-1}, correspond to the symmetric and asymmetric stretching of OH. The observed band at 3167 cm^{-1} in experimental IR is assigned to the stretching of C–H (ring). Furthermore, the band around 3064 cm^{-1} is attributed to the N–H stretching mode. However, the bands located at 3043 cm^{-1} and 2925 cm^{-1} in FT-IR are due to the asymmetric and symmetric stretching vibration of CH_2. In addition, the band located at 1549 cm^{-1} is attributed to the CH_2 deformation. The band located around 1729 cm^{-1} is attributed to ring deformation. The band observed at 1627 cm^{-1}

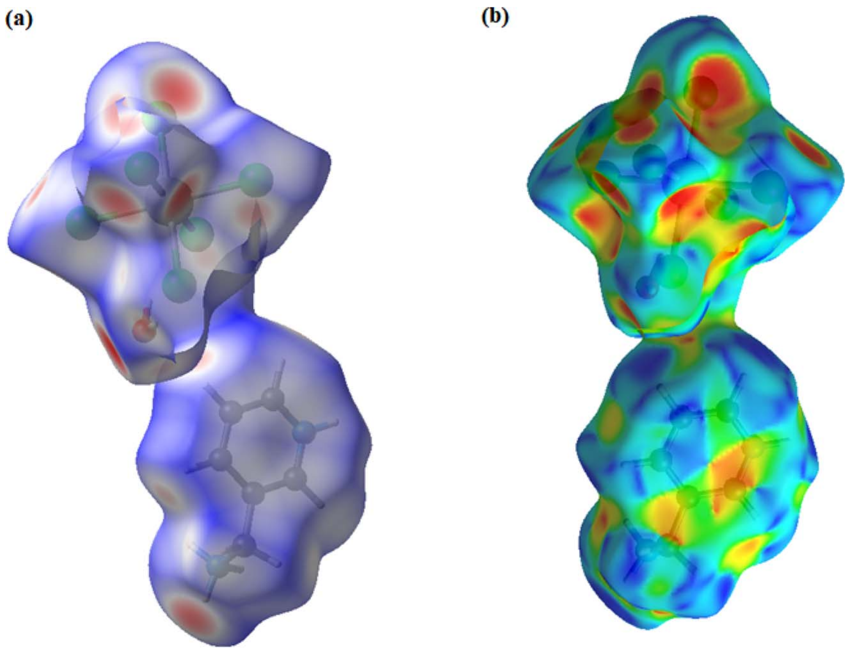

Fig. 3 Hirshfeld surface (a) mapped to d_{norm} (b) shape index.

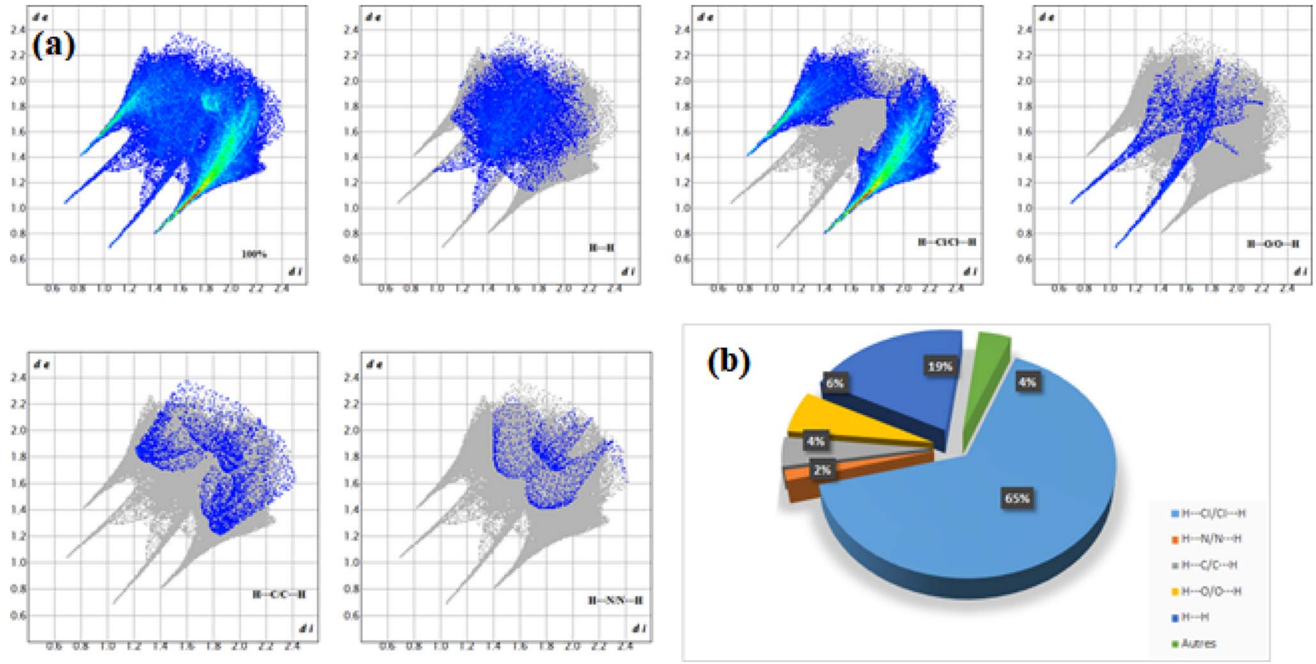

Fig. 4 (a) Fingerprints of interatomic contacts and Hirshfeld surfaces in d_{norm}; (b) relative contribution of different contacts.

in infrared corresponds to the H–N–H in plane bending. However, the band located at 1602 cm^{-1} is assigned to the (C–C) stretching, in plane bending of H–N–C and H–C–C. Nevertheless, the C–C–C (ring) deformation wavenumbers attributed at 1580 cm^{-1}. In fact, the H–C–H in the plane-bending vibration is observed at 1483 cm^{-1}. The band located at 1390 cm^{-1} in FT-IR is assigned to the H–C–C–N torsion. However, the bands observed at 1379 cm^{-1} and 1317 cm^{-1} in infrared correspond to N–C stretching while the C–N elongation observed at 972 cm^{-1} and the symmetric CCN stretching is observed at 1091 cm^{-1}. The band observed at 1182 cm^{-1} is attributed to the C–C–N deformation. The bands located around 1050 and 793 cm^{-1} are attributed to the H–C–C–H torsion. In fact, the OH (H_2O) bending vibration is observed at 566 cm^{-1}. Finally, the bands that appear at 494 cm^{-1} and 416 cm^{-1} are attributed to the H–C–C–C torsion and C–C–C–C torsion, respectively.

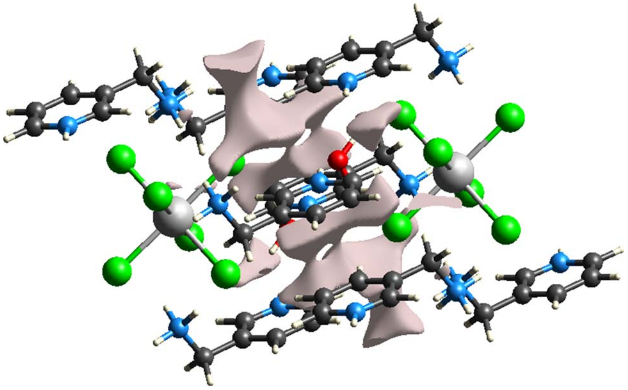

Fig. 5 The surface area of voids in the structure of the compound $(C_6H_{10}N_2)_2[PdCl_6]\cdot 2H_2O$.

Table 6 The electric dipole moment, the average polarizability, and second hyperpolarizability

Dipole moment (D)		Second hyperpolarizability (10^{-36} esu)	
μ_x	8.40	γ_{xxxx}	3.19
μ_y	17.14	γ_{yyyy}	2.32
μ_z	1.58	γ_{zzzz}	0.71
μ_{tot}	19.16	γ_{xxxy}	0.12
Polarizability (10^{-24} esu)		γ_{yyyx}	0.04
α_{xx}	25.02	γ_{xxxz}	0.11
α_{yy}	19.05	γ_{yyyz}	0.11
α_{zz}	26.61	γ_{xxyy}	0.94
α_{xy}	3.84	γ_{xxzz}	0.60
α_{xz}	0.62	γ_{yyzz}	0.51
α_{yz}	0.33	γ	2.06
α_{tot}	23.56		

3.4. Optical absorption

The UV-visible spectra of the organic molecule 3-AMP and $(3\text{-AMP})_2[PdCl_6]\cdot 2H_2O$ complex are shown in Fig. 7. The data is depicted as a function of wavelength (190–800 nm). From these spectra, we observed six clear peaks located at $\lambda = 430$ nm. The initial peak observed at $\lambda = 355$ nm is attributed to $\pi \rightarrow \pi^*$ transitions involving the ring in the organic cation. This peak is also visible in the spectrum of the cation at 206 nm. The peaks centered at $\lambda_2 = 218$ nm, $\lambda_3 = 238$ nm, $\lambda_4 = 253$ nm, and $\lambda_5 = 276$ nm are attributed to $n \rightarrow \pi^*$ transitions involving the ring within the organic cation. Charge transfer from the organic to inorganic part in $(3\text{-AMP})_2[PdCl_6]\cdot 2H_2O$ complex can be assigned to the strong peak at $\lambda_6 = 294$ nm. The optical absorption coefficient (α) and the band gap energy (E_g) are the most critical parameters. To determine the band gap energy of our complex an accurate spectrophotometric method has been applied using the Tauc relationship given by this formula:

$$\alpha \hbar \nu = C(h\nu - E_g)^n \tag{2}$$

where α, h, C, ν, E_g are the absorption coefficient, the Planck's constant, the absorption constant, the light frequency, and the optical band gap energy, respectively. Such that the optical absorption coefficient (cm^{-1}) was derived from the absorbance using the following correlation:[44]

$$\alpha = \frac{2.303A}{t} \tag{3}$$

where; t is the sample thickness and A is the absorbance.

Moreover, the optical band gap value is determined by extending the linear segment of the plot along the energy axis,

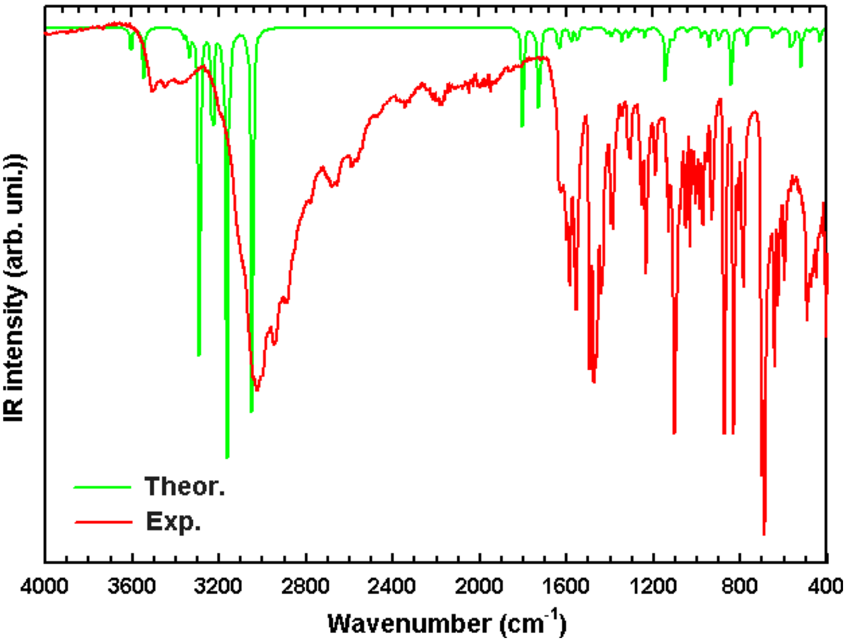

Fig. 6 Superposition of the experimental (red) and the DFT computed (green) FT-IR spectra of $(C_6H_{10}N_2)_2[PdCl_6]\cdot 2H_2O$ in the 400–4000 cm^{-1} region.

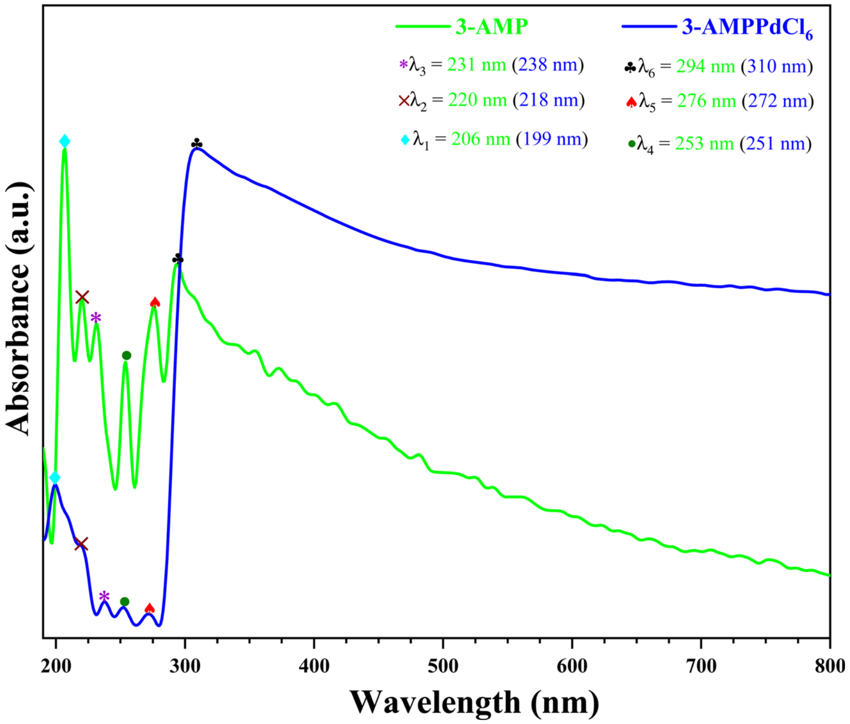

Fig. 7 Experimental and simulated optical absorption spectra of $C_6H_{10}N_2$ and $(C_6H_{10}N_2)_2[PdCl_6]\cdot 2H_2O$.

where $(\alpha h\nu)^2 = 0$ using the Tauc model. The curves $(\alpha h\nu)^2$ as a function of $h\nu$ for the organic molecule 3-AMP and $(3\text{-AMP})_2[PdCl_6]\cdot 2H_2O$ complex are shown in Fig. 8. Thus, the linear interpolation on the x-axis of the graph $(\alpha h\nu)^2$ is used to determine the band gap energy, which is approximated at 3.15 eV and 2.35 eV, respectively. These energies can classify this material as a semiconductor.

3.5. Frontier molecular orbital analysis

We conducted a comprehensive investigation of the optical properties and chemical stability by analyzing the energies of the highest occupied molecular orbital (HOMO) and lowest unoccupied molecular orbital (LUMO), along with the boundary molecular orbitals, using the TD-DFT method. The latter plays an interesting role in electrical, optical properties and in chemical

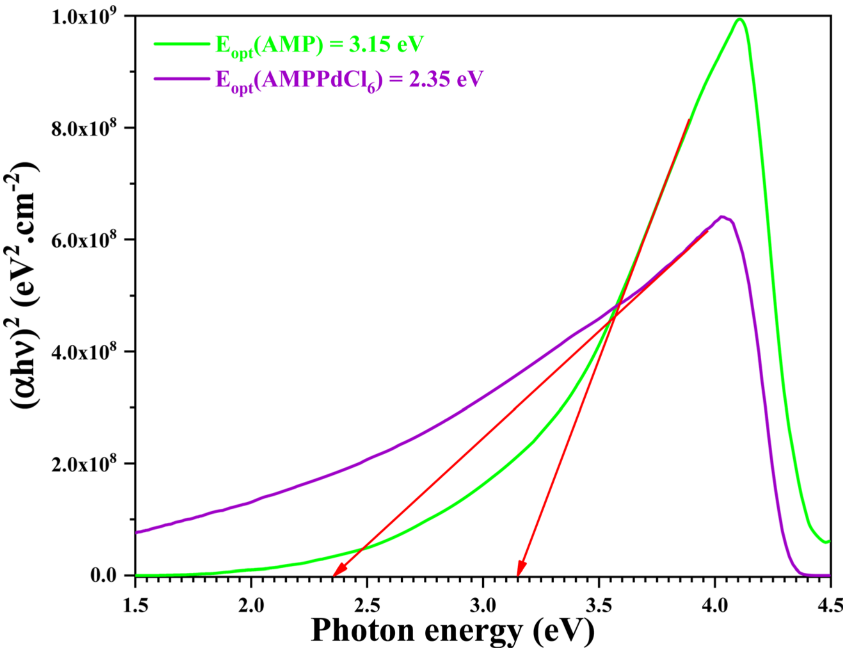

Fig. 8 Optical band gap determination of $C_6H_{10}N_2$ and $(C_6H_{10}N_2)_2[PdCl_6]\cdot 2H_2O$.

reactions.[45] The electronic distribution of the molecular orbitals of the compound studied is shown in Fig. 9. HOMO and LUMO energies are used to determine global reactivity descriptors, such as ionization potential (IP), electron affinity (EA), electrophile index (ω), chemical potential (μ), electronegativity (χ) and hardness (η). In simple molecular orbital theory approaches, the HOMO energy (E_{HOMO}) is related to (IP) and the energy of LUMO (E_{LUMO}) is linked to (EA) by Koopmann's theorem.[46,47] The key parameter for confirming the stability of our investigated compound is $\Delta E_{\mathrm{H-L}}$, this energy found as 1.72 eV. These parameters are computed based on the following equations and presented in Table 5:

$$\Delta E_{\mathrm{H-L}} = E_{\mathrm{LUMO}} - E_{\mathrm{HOMO}} \tag{4}$$

$$I_{\mathrm{P}} = -E_{\mathrm{HOMO}} \tag{5}$$

$$E_{\mathrm{A}} = -E_{\mathrm{LUMO}} \tag{6}$$

$$\chi = -\frac{E_{\mathrm{LUMO}} + E_{\mathrm{HOMO}}}{2} \tag{7}$$

$$\mu = \frac{E_{\mathrm{LUMO}} + E_{\mathrm{HOMO}}}{2} \tag{8}$$

$$\eta = \frac{E_{\mathrm{LUMO}} - E_{\mathrm{HOMO}}}{2} \tag{9}$$

$$\omega = \frac{\mu^2}{2\eta} \tag{10}$$

3.6. Fluorescence property

Additionally, we investigated the luminescent properties of the compound at room temperature. Fig. 10 illustrates the fluorescence spectrum of $(C_6H_{10}N_2)_2[PdCl_6]\cdot 2H_2O$ observed in the solid state at room temperature, with excitation at 227 nm. The result showed a wide fluorescence band from 440 nm to 700 nm.

When excited with 227 nm light, the established compound displays vibrant blue-violet, green, and orange emissions in aggregated states, collectively forming the components of white light. The CIE coordinates (0.3569, 0.3915) define a triangular area encompassing the white light energy point (0.33, 0.33) on the CIE chromaticity diagram. This compound's emission covers nearly the entire visible light spectrum, resulting in a pure white light.

3.7. Electrochemical behavior

The electrochemical studies of $(3\text{-AMP})_2[PdCl_6]\cdot 2H_2O$ were conducted in a distilled water aqueous solution (10^{-3} mol L^{-1}) within a potential range from -600 to 1200 mV at a scan rate of 100 mV s^{-1}. The voltammetric pattern displayed a single redox wave, attributed to the palladium redox process (Fig. 11). Due to the limited reversibility of the waves, we were able to ascertain the average peak potentials between the respective anodic and cathodic peaks $E_{1/2}$. The mean peak potential $E_{1/2} = (E_{\mathrm{pa}} + E_{\mathrm{pc}})/2$ is +0.61 V. The reduction step involves 2 electrons, calculated from the equation $E_{\mathrm{p}}\ (\mathrm{V}) = 0.06/n$. Hence, we deduce that the reduction is a one-reversible, one-electron process. Electrochemical band gaps (E'_{g}) are determined from the cyclic voltammetry (CV) measurements using the following equations:[48]

$$E_{\mathrm{HOMO}} = -(4.39 + E_{\mathrm{ox}}) \tag{11}$$

$$E_{\mathrm{LUMO}} = -(4.39 + E_{\mathrm{red}}) \tag{12}$$

$$E'_{\mathrm{g}} = E_{\mathrm{LUMO}} - E_{\mathrm{HOMO}} \tag{13}$$

where E_{ox} is the oxidation peak potential and E_{red} is the reduction peak potential. The electrochemical band gap (E'_{g}) between HOMO–LUMO energy levels is 1.32 eV. The complex's oxidation and reduction characteristics explains the stability of the metal ion.

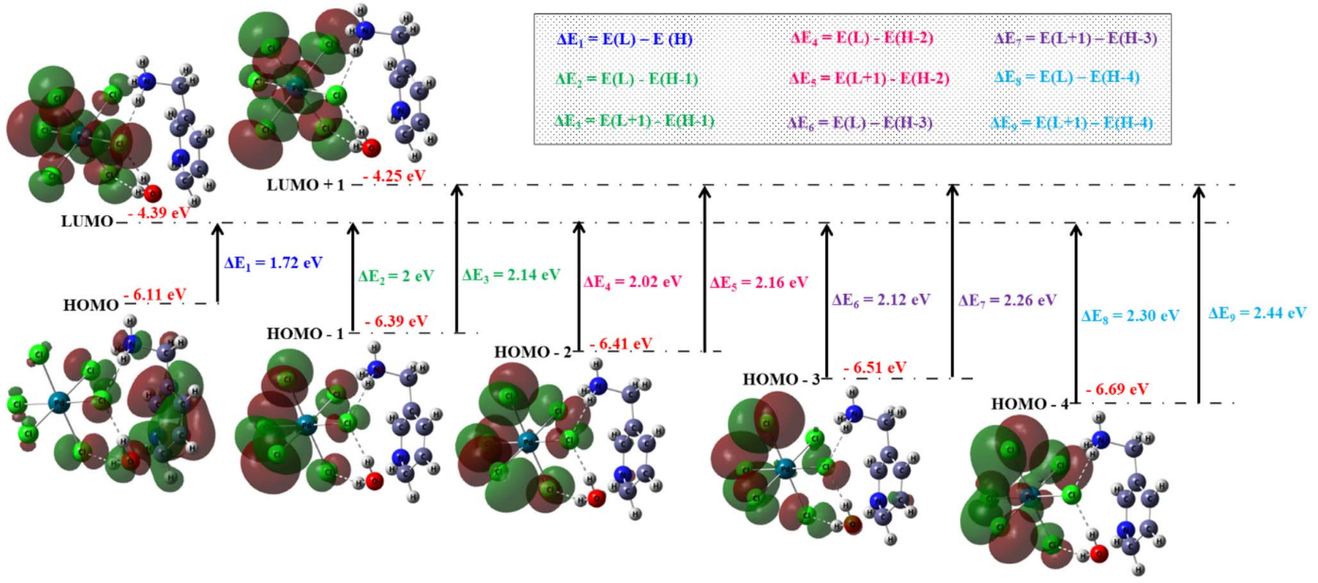

Fig. 9 Frontier molecular orbitals involved in some computed transitions of $(C_6H_{10}N_2)_2[PdCl_6]\cdot 2H_2O$.

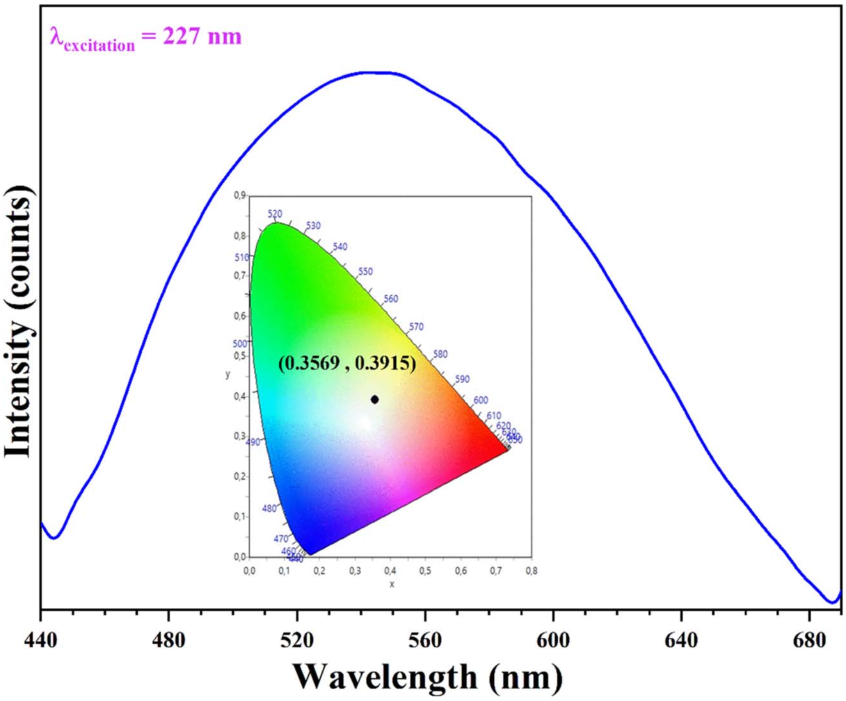

Fig. 10 Emission spectrum of $(C_6H_{10}N_2)_2[PdCl_6]\cdot 2H_2O$.

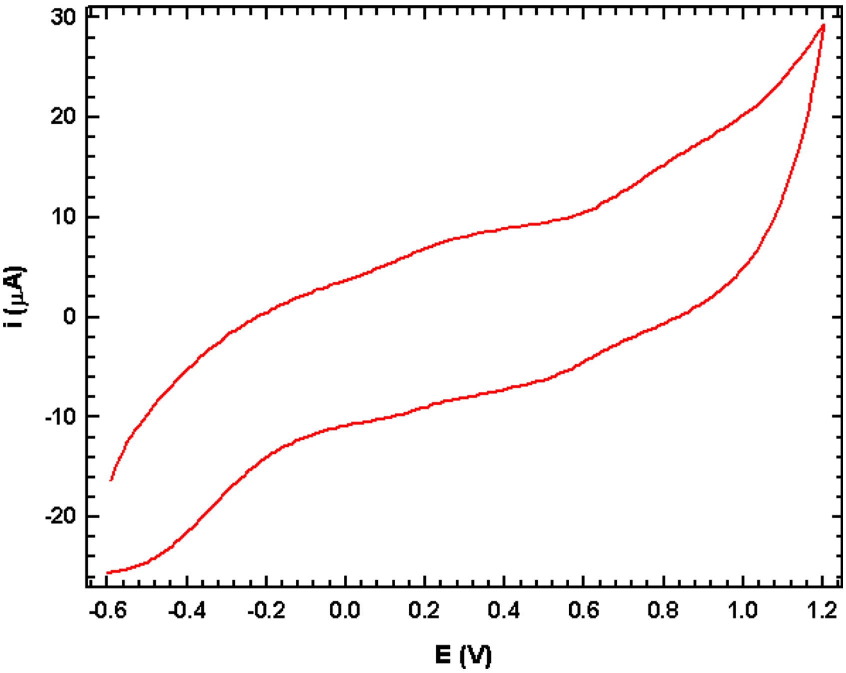

Fig. 11 Cyclic voltammogram of $(C_6H_{10}N_2)_2[PdCl_6]\cdot 2H_2O$ (scan rate 100 mV s^{-1}).

3.8. Thermal analysis

The crystals' thermal stability was investigated through simultaneous thermogravimetric analysis and measurements of differential thermal analysis (TGA-DTA) simultaneously for the synthesized compound, carried out at a specified heating rate of 5 °C min^{-1} from 25 to 550 °C, is depicted in Fig. 12.

According to the TGA curve, compound $(C_6H_{10}N_2)_2[PdCl_6]\cdot 2H_2O$ does not show any mass loss before 230 °C, beyond this temperature, the sample undergoes continuous decomposition. The first thermal phenomenon undergone by our compound is located between 25 and 110 °C, associated with a more intense endothermic peak around 85 °C, and corresponds to the

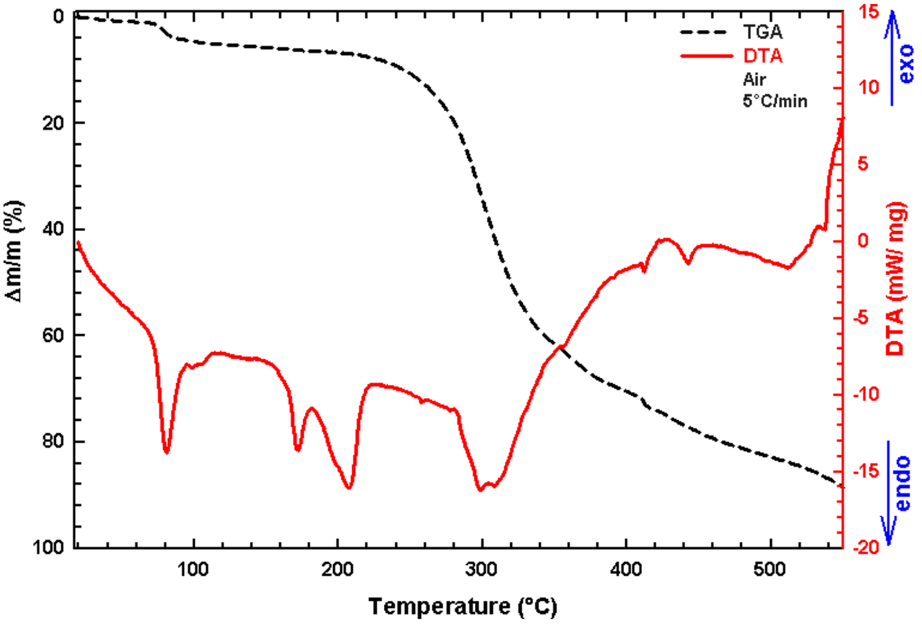

Fig. 12 Thermogravimetric and differential thermal analysis plots for $(C_6H_{10}N_2)_2[PdCl_6]\cdot 2H_2O$. The scan was performed in flowing air with a ramp rate of 5 °C min^{-1}.

departure of two water molecules, indicated by a weight loss of 5.86%, which aligns with the calculated weight loss (6.25%) and formation of the anhydrous phase $(C_6H_{10}N_2)_2[PdCl_6]$. In the 210 °C to 350 °C temperature range, an endothermic peak accompanies a weight loss observed on the TGA curve at around 305 °C. During this process, the material theoretically corresponds to 61.48% of the total mass. This loss is ascribed to the degradation of two organic molecules and the volatilization of two Cl_2 molecules, the compound formed as a result of this mass loss is represented by the chemical formula $[PdCl_2]$. From 350 °C, the compound continues to decompose with a mass loss of two chloride ions, ultimately resulting in the formation of palladium oxide (PdO) as the end product.

3.9. Dielectric studies

3.9.1. Dielectric constant. Fig. 13 shows the frequency dependence of the real part (ε') of the dielectric permittivity for the studied material at different temperatures. The dielectric

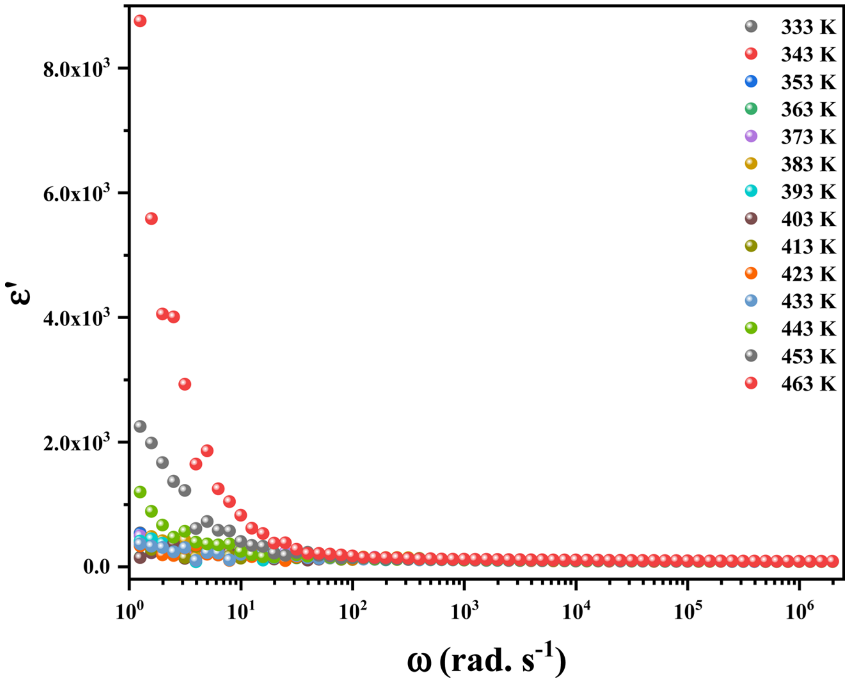

Fig. 13 The variation of the real part of the permittivity of $(C_6H_{10}N_2)_2[PdCl_6]\cdot 2H_2O$ sample.

constant shows a significant rise at low frequencies, and this rise alters in shape with temperature variations, attributed to the motion of conducting ions. However, the ε' values decrease with increasing frequency ($f > 10^2$ Hz) and almost reach a plateau, enhancing the capacity for storing energy.[49] Moreover, the dielectric constant values increase with temperature at a specific frequency. The dielectric characteristics observed in this material is due to the Maxwell–Wagner type interfacial polarization.[50]

3.9.2. Dielectric loss factor. Investigating the "dissipation factor" in materials intended for optoelectronic applications, as illustrated by tan(δ) in Fig. 14, was crucial. The dielectric loss mainly arises from several physical phenomena, including the conduction process, molecular dipole moment, dielectric relaxation, and interfacial polarization.[51] This factor can be computed based on:

$$\tan(\delta) = \frac{\varepsilon''}{\varepsilon'} \tag{14}$$

With increasing temperature, the dielectric loss shifts towards higher frequencies, signifying the thermal activation of polarization. This advancement has prompted the consideration of these materials for use in electrical devices.[52] Moreover, it suggests that elevated temperatures and lower frequencies lead to heightened dielectric loss, offering a clear indication of enhanced conductivity in the materials.[53]

3.9.3. Impedance spectroscopy analysis. Impedance spectroscopy is a widely recognized method for examining the electrical properties of a material. For that, complex impedance spectra $-Z'' = f(Z')$ of the $(C_6H_{10}N_2)_2[PdCl_6]\cdot 2H_2O$ compound were measured at various temperatures (333–463 K) as shown in Fig. 15. These diagrams confirm the presence of characteristic semi-circular patterns, positioned below the horizontal axis, which diminish noticeably with rising temperature, suggesting a relaxation mechanism that deviates from the Debye type.[54]

As shown in Fig. 16a, it is clear that the amplitude of the real parts, denoted as Z' and representing electrical resistance, decreases with increasing frequency and temperature. This phenomenon involves the negative temperature coefficient of resistance (NTCR) in the $(C_6H_{10}N_2)_2[PdCl_6]\cdot 2H_2O$ compound. At higher frequencies, the Z'' values for all temperatures converge to a single point, suggesting a potential discharge of space charge and consequently lower energy barrier characteristics.

Examining the change in Z'' (see Fig. 16b) with angular frequency reveals the emergence of singular peaks at specific frequencies, along with a reduction in peak height as the temperature increases. Additionally, we observed peak broadening with a decrease in the value of $Z''_{\max}$, implying an escalating loss in the resistive properties of the sample.

3.9.4. Complex modulus analysis. We have also examined the electrical modulus to explore the relaxation mechanism in the hybrid material $(C_6H_{10}N_2)_2[PdCl_6]\cdot 2H_2O$. This offers valuable insights into various aspects including the electrode effect, grain boundary effect, grain characteristics, conductivity, and relaxation behavior of the material. This compound is depicted by the equation: $M = M' + iM''$. The formula below has been utilized to determine M':

$$M' = \frac{\varepsilon'}{\varepsilon'^2 + \varepsilon''^2} \tag{15}$$

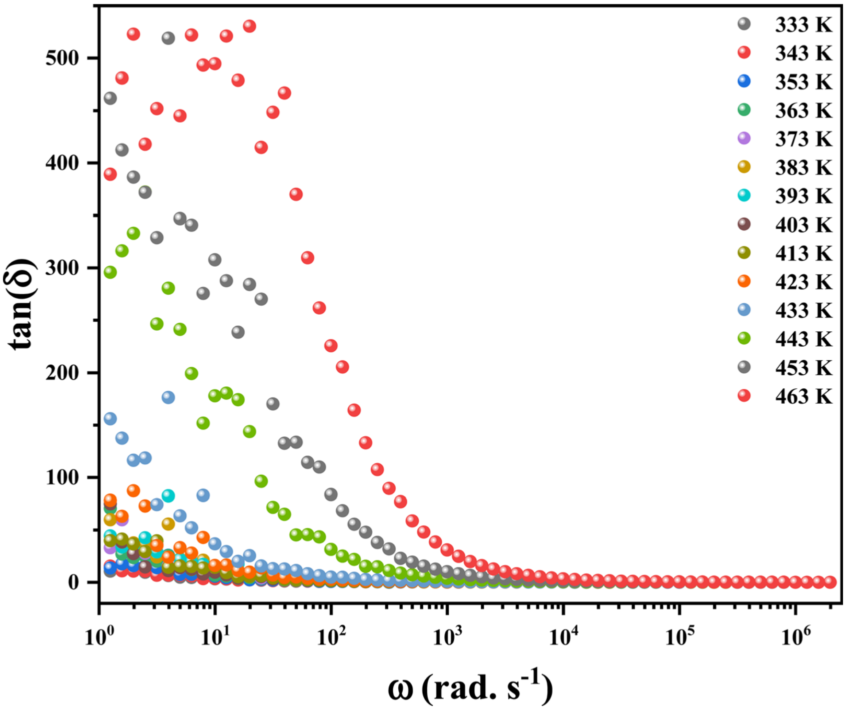

Fig. 14 The variation of the dielectric loss factor at different temperatures.

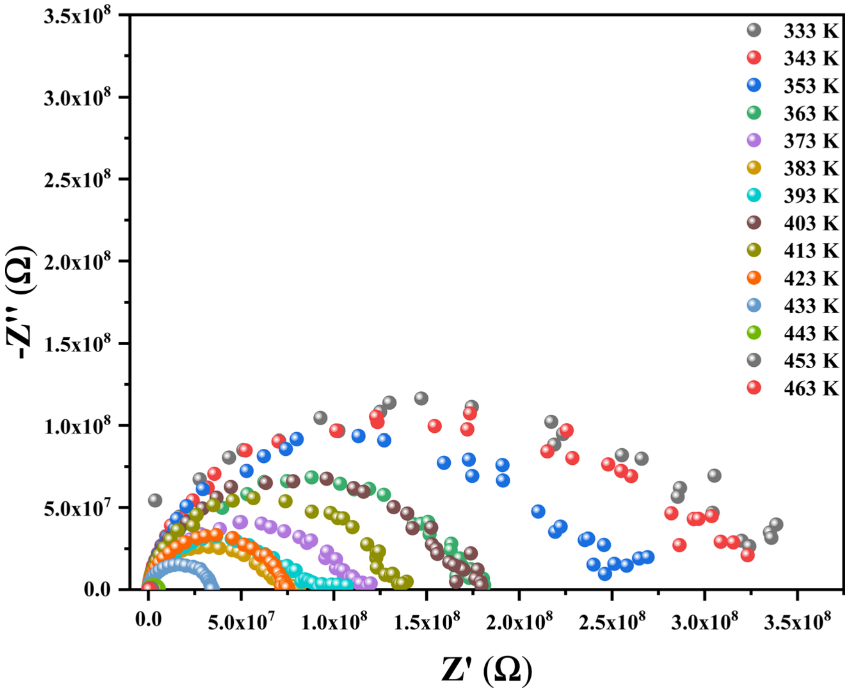

Fig. 15 Nyquist plots of the compound at room temperature.

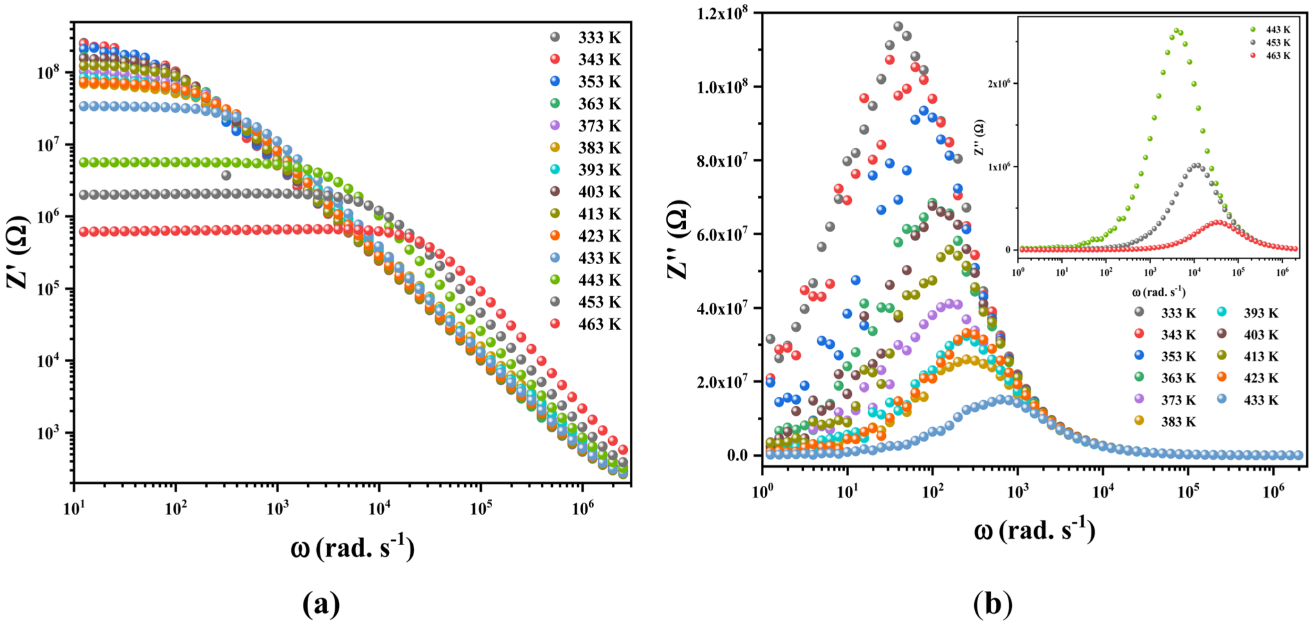

Fig. 16 The frequency dependence of Z' (a) and Z'' (b) at different temperatures for $(C_6H_{10}H_2)_2[PdCl_6]\cdot 2H_2O$ crystal.

Fig. 17a illustrates the frequency-dependent behavior of the real components of the modulus spectra $M'(T, f)$ within the temperature range of 333 to 463 K. At all temperatures, M' increases as frequency rises. At low frequencies, M' approaches zero, indicating no electrode influence. Fig. 17b demonstrates the change in the imaginary part of the electric modulus (M'') with frequency at various temperatures. The M'' value exhibited a consistent increase with the rising frequency, reaching its maximum ($M''_{\max}$), and then rapidly declining, as illustrated in this graph. As the temperature rises, the peak shifts towards higher frequencies, suggesting the occurrence of a relaxation process. At low frequencies, M'' values approach zero, indicating that the electrode influence can be ignored.[55] The approximation of the imaginary part of $M''(\omega)$ is proposed by Bregman:[56]

$$M'' = \frac{M''_{\max}}{1-\beta+\left(\frac{\beta}{1+\beta}\right)\left[\beta\left(\frac{\omega_{\max}}{\omega}\right)+\left(\frac{\omega}{\omega_{\max}}\right)^{\beta}\right]} \qquad (16)$$

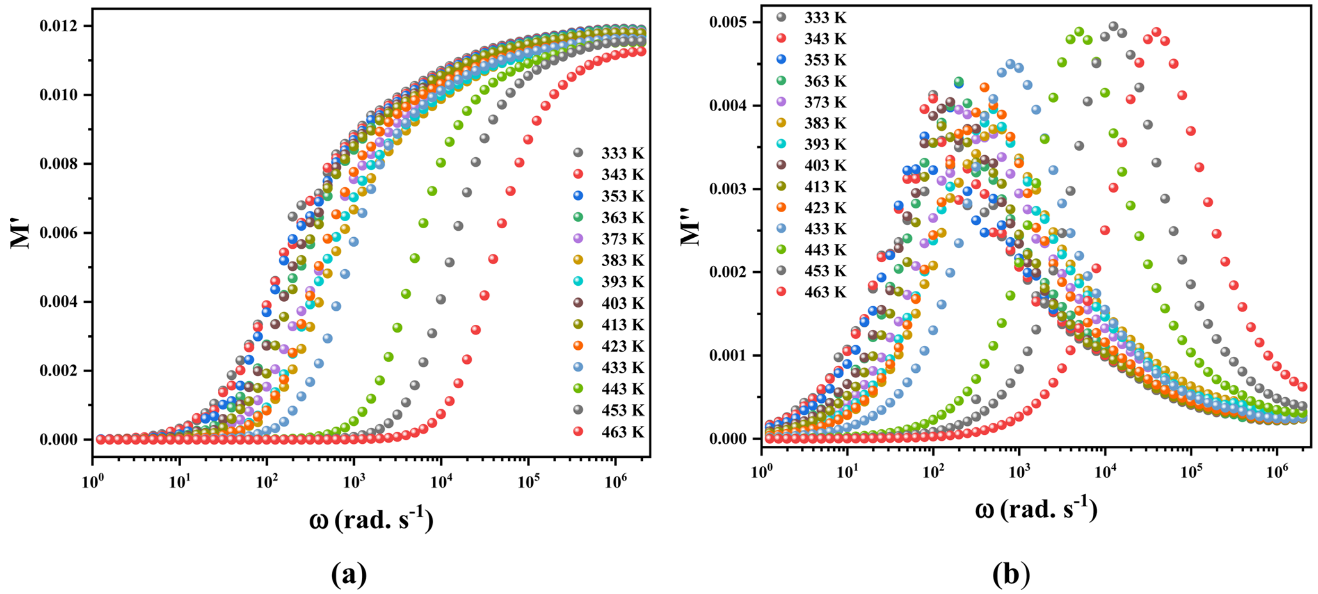

Fig. 17 Frequency dependent of M' (a) and M'' (b) at different temperatures for $(C_6H_{10}N_2)_2[PdCl_6]\cdot 2H_2O$.

where, ω_{max} is the frequency at which the maximum modulus M''_{max} occurs, and β suggests the importance of coupling between mobile ions in the conduction process, falling within the range of (0–1). To understand the effects of clear grain and grain boundaries, we utilized master modulus spectra in $M'' = f(M')$. Fig. 18 exhibits the complex modulus spectrum of $(C_6H_{10}N_2)_2$ $[PdCl_6]\cdot 2H_2O$ at specified temperatures. It reveals a multiple semicircular arc, with the point of intersection on the real axis signifying the capacitive contribution of the grains. The arcs overlapped, creating a curve, suggesting that the underlying conduction mechanism remains unchanged.

3.9.5. Conductivity study. AC conductivity analysis aids in determining the mode of transport for charge carriers, which governs the conduction process and its variation with frequency and temperature. The frequency dependence of AC conductivity for the $(C_6H_{10}N_2)_2$ $[PdCl_6]\cdot 2H_2O$ sample is documented in Fig. 19. The AC conductivity rises as the frequency increases. The conductivity spectra can be characterized by two regions: the first, at low frequencies, a plateau is remarked as described through the initial term of the Jonscher equation, which defines the direct current conductivity (dc) is present.

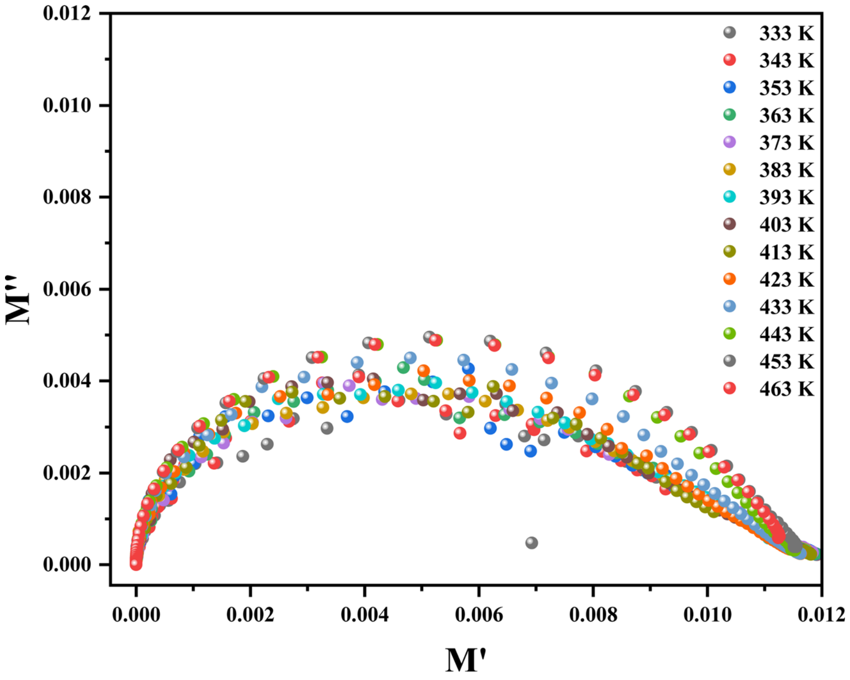

Fig. 18 Complex modulus spectra at 333–463 K.

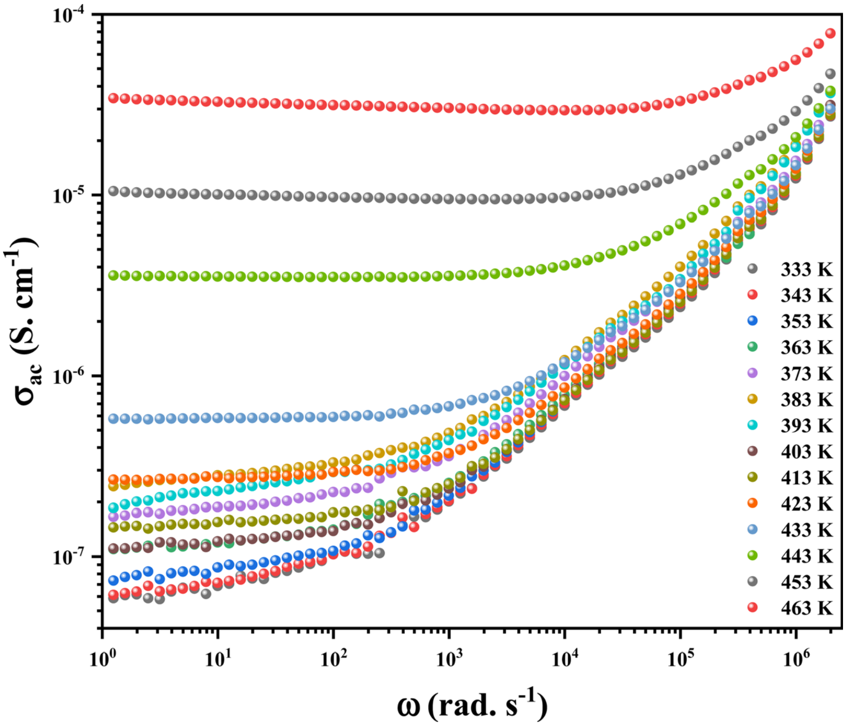

Fig. 19 Frequency dependence of AC conductivity at various temperatures.

Secondly, at high frequencies, the conductivity demonstrates an asymptotic form, known as the dispersive regime, characterized by the second term $A\omega^S$, representing the charge species accumulated at the grain boundaries. These species possess enough energy to surpass the energy barrier with increasing temperature. This variation follows the Jonscher power law:[57]

$$\sigma_{ac}(\omega) = \sigma_{dc} + A\omega \tag{17}$$

The expression involves σ_{ac}, the conductivity of the alternating current, σ_{dc} the frequency-independent conductivity obtainable by extending the low-frequency plateau to zero frequency, A, a temperature-dependent constant determining the polarization strength, and $|s|$, the power law exponent typically falling within the range $1 < s < 2$.[58] The diminished energy gap (3.56 eV) and elevated conductivity, approximately 10^{-4} Ω^{-1} cm^{-1}, establish that this material is a semiconductor suitable for application in photovoltaic cells, serving as a photodetector that transforms optical signals into electrical signals. An essential characteristic that classifies this material as an optoelectronic material is its thermal stability, which extends up to 483 K, credited to the presence of palladium.

3.10. Biological activities

The results of this study show that consumption of ethanol induces the recruitment of neutrophils to the stomach tissues, which causes ulceration. This is indicated by a marked increase in gastric juice MPO activity, which in turn causes an increase in oxidative stress, as evidenced by a marked increase in gastric juice TBARS levels. Damage to the stomach mucosa tissues was produced by both inflammation and oxidative stress. On the other hand, there was a noticeable protective effect against this oxidative stress when 3-AMP was given *via* gastric gavage to ulcerated rats. This was demonstrated by a notable 26 and 58% decrease in TBARS after ingestion of 3-AMP compounds at doses 50 and 100 mg kg^{-1}. This compound's anti-inflammatory and anti-oxidant effects shield stomach mucosa against damage and erosion, as evidenced by a significant decrease in stomach ulcer area by 16 and 30% following the consumption of 3-AMP supplements at doses of 50 and 100 mg kg^{-1} respectively. Certainly, our study unequivocally demonstrates that the intake of this compound safeguards against damage and ulceration of gastric tissues through two distinct mechanisms. First, it induces and stimulates the antioxidant system within gastric tissues, leading to the neutralization and suppression of free radicals. This, in turn, protects against cellular damage, as evidenced by the reduction in TBARS levels in gastric juice. Second, the compound inhibits the pivotal inflammatory enzyme, specifically the activity of MPO, subsequently impeding inflammatory cascades and, thereby, protecting against gastric tissue ulceration. Additionally, prior research has revealed alternative mechanisms of compounds containing palladium, including the suppression of inflammatory reaction mediators,[14–16] reduction in pro-inflammatory cytokines, and nitrite production. Simultaneously, these compounds enhance the activity of antioxidant enzymes.[59,60] In addition, compounds containing different polyphenolic chemicals have been shown to target particular molecules and modify a variety of signaling pathways, resulting in varied physiological effects. One such example of an active component for the treatment of inflammation is the phenolic compound's ability to block the NF-κB pathway, which has anti-inflammatory properties (Fig. 20).[61,62]

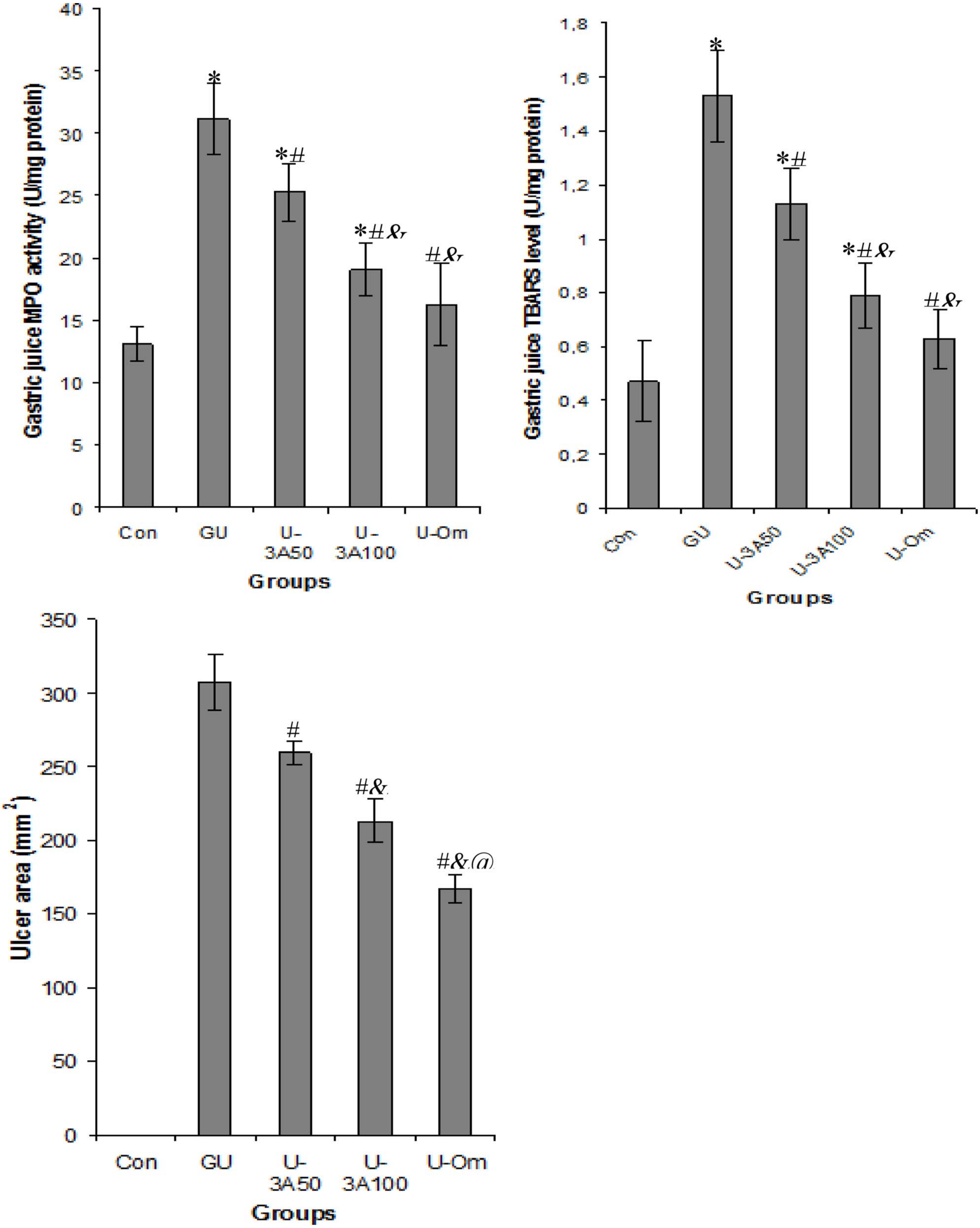

Fig. 20 Effects of new palladium(II) halide complex on key indice related to inflammation as MPO activity, to stress as TBARS rates and gastric ulcer as ulcer area (mm^2). *$P < 0.05$ significant differences compared to controls; $^{\#}P < 0.05$ significant differences compared to ulcerated rats; $^{\&}P < 0.05$ significant differences compared to ulcerated rats treated with palladium(II) halide complex at dose 50 mg kg^{-1} (3A_{50}); $^{@}P < 0.05$ significant differences compared to ulcerated rats treated with palladium(II) halide complex at dose 50 mg kg^{-1} (3A_{100}).

4 Conclusion

In summary, this paper focuses on the synthesis and characterization of a novel hybrid compound. The compound was synthesized using slow evaporation conditions and characterized through various techniques including single-crystal X-ray diffraction, electrochemical analysis, spectroscopic studies, and thermal analysis. The structural, vibrational, and optical spectra (UV-Vis, PL, HOMO–LUMO), calculated using the DFT/B3LYP/Lanl2mb level of theory, align well with experimental findings. Analysis of the X-ray diffraction data reveals that the grown crystal possesses a triclinic structure with a centrosymmetric space group $P\bar{1}$.

The crystal structure is made up of organic $[C_6H_{10}N_2]^{2+}$ entities, which are connected by weak hydrogen bonds to $[PdCl_6]^{4-}$ anions and free water molecules, creating a three-dimensional network. The crystal's cohesion is ensured by a three-dimensional system of hydrogen bonds. The optical properties have good transparency in the visible region and are suitable for use in nonlinear optics devices. The UV-visible spectra analysis reveals a band gap energy of 2.35 eV for the title compound. In addition, analysis of the HOMO and LUMO energy levels yields a gap energy (E_g) of 3.56 eV, along with determination of global reactivity descriptors such as ionization potential (IP), electron affinity (EA), electrophile index (ω), chemical potential (μ), electronegativity (χ), and hardness (η). Furthermore, understanding of the stability of the metal ion is enhanced by examining the oxidation and reduction behavior of the complex.

Moreover, at room temperature, the investigated compound displays blue luminescence. Thermal analyses indicate that the thermal decomposition of the palladium complex takes place in several stages: the first involves dehydration, leading to the formation of the anhydrous phase $(C_6H_{10}N_2)_2[PdCl_6]$. The second one pertains to the decomposition of two organic molecules and the evaporation of four chloride ions, probably in the form $(C_6H_8N_2Cl)_2\cdot(HCl)_2$, leading to $PdCl_2$, and the last corresponds to the decomposition of palladium dichloride to its oxide PdO. The considerable dielectric permittivity, strong capacitance, elevated conductivity, and minimal dielectric loss of this material render it exceptionally adaptable for FET (Field-Effect Transistor) applications when compared to alternative dielectric materials. The current research underscores the need for additional investigations into these novel materials, potentially leading to the development of new drugs targeting inflammation, oxidation, and gastric issues. While the compound $(C_6H_{10}N_2)_2[PdCl_6]\cdot 2H_2O$ shows promise, additional research is required to thoroughly explore its potential utility and application in various fields, such as catalysis.

Author contributions

Sarra Bougossa: formal analysis, writing – original draft; Noureddine Mhadhbi, Mohamed Hamdi: writing, investigation, validation; Ali Ben Ahmed, Khaled Hamden, Abderrazek Oueslati: review & editing, visualization, data curation; Kais Elghniji, Jeanneau Erwann: data curation, methodology, resources; Houcine Naïli: project administration, validation, supervision.

Conflicts of interest

The authors declare no competing financial interest.

Acknowledgements

The authors extend their appreciation to the Deanship of Scientific Research at Northern Border University, Arar, KSA for funding this research work through the project number “NBU-FFR-2024-2924-04”.

References

1 C.-B.-C. Sanchez, S. Cassaignon, C. Chaneac, O. Durupthy, M. Faustini, D. Grosso., C. Laberty-Robert, L. Nicole, D. Portehault, F. Ribot, L. Rozes and C. Sassoye, Molecular Engineering of Functional Inorganic and Hybrid Materials, *Chem. Mater.*, 2014, **26**, 221–238.

2 S. Boufas, N. Mohamedi, P. Bénard-Rocherullé, P. Roussel and T. Roisnel, $CdCl_3-$ vs $CdCl_4^{2-}$ in Hybrid Materials, *Procedia. Soc. Behav. Sci.*, 2015, **195**, 1639–1647.

3 T. Sekine, T. Okuno and K. Awaga, *Mol. Cryst. Liq. Cryst. Sci. Technol., Sect. A*, 1996, **279**, 65–72.

4 W.-Q. Chen, M.-H. Feng, D.-D. Zhou, Y.-Q. Peng, S. Han, X.-P. Liu, L.-M. Yang, J.-R. Zhou and C.-L. Ni, *Synth. React. Inorg., Met.-Org., Nano-Met. Chem.*, 2012, **42**(6), 811–817.

5 M. Mathlouthi, E.-J. Daron, M. Rzaigui and W. Smirani, *J. Supercond. Novel Magn.*, 2016, **29**, 1573–1581.

6 D.-B. Mitzi, C.-D. Dimitrakopoulos and L.-L. Kosbar, Structurally Tailored Organic−Inorganic Perovskites: Optical Properties and Solution-Processed Channel Materials for Thin-Film Transistors, *Chem. Mater.*, 2001, **13**(10), 3728–3740.

7 S. Weina, H. Chunyin, Z. Wang, G. Yachen, Y. Yixiao, W. Yiqun, C. Zhimin, L. Xiaochen and D. Yongli, *Carbon*, 2014, **77**, 1020–1030.

8 M.-D. Birowosuto, D. Cortecchia, W. Drozdowski, K. Brylew, W. Lachmanski, A. Bruno and C. Soci, X-ray Scintillation in Lead Halide Perovskite Crystals, *Sci. Rep.*, 2016, **6**(1), 37254.

9 Y. Tominaga and H. Ohno, Lithium ion conduction in linear- and network-type polymers of PEO/sulfonamide salt hybrid, *Electrochim. Acta*, 2000, **45**(19), 3081–3086.

10 L. M. Novena, S. S. Kumar and S. Athimoolam, Improved solubility and bioactivity of theophylline (a bronchodilator drug) through its new nitrate salt analysed by experimental and theoretical approaches,*J. Mol. Struct.*, 2016, **1116**, 45–55.

11 S. Gatfaoui, A. Sagaama, N. Issaoui, T. Roisnel and H. Marouani, Synthesis, experimental, theoretical study and molecular docking of 1-ethylpiperazine-1,4-diium bis(nitrate), *Solid State Sci.*, 2020, 106326.

12 R. G. Lacoste and A. E. Marttel, New Multidentate Ligands. I. Coordinating Tendencies of Polyamines Containmg α-

Pyridyl Groups with Divalent Metal Ions, *Inorg. Chem.*, 1964, **3**(6), 881–884.

13 T. M. Hseu, Y. H. Tsai and C. W. Cheng, Spectrophotometric Studies of Nickel(II) Chelate of 2-Picolylamine, *J. Chin. Chem. Soc.*, 1975, **22**(4), 299–308.

14 S. Bhuvaneswari, M. Umadevi and R. Vanajothi, Effects on Anti-Inflammatory, DNA Binding and Molecular Docking Properties of 2-Chloroquinolin-3-Yl-Methylene-Pyridine/Pyrazole Derivatives and Their Palladium (II) Complexes, *Bioorg. Med. Chem. Lett.*, 2020, **30**, 127593.

15 M. Naveed, R. Ullah, A. Khan, B. Shal, A. U. Khan, S. Z. Khan, Z. U. Rehman and S. Khan, Anti-Neuropathic Pain Activity of a Cationic Palladium (II) Dithiocarbamate by Suppressing the Inflammatory Mediators in Paclitaxel-Induced Neuropathic Pain Model, *Mol. Biol. Rep.*, 2021, **48**, 7647–7656.

16 M. Naveed, S. Z. Khan, S. Zeeshan, A. Khan, B. Shal, A. Atiq, H. Ali, R. Ullah and S. Khan, A New Cationic Palladium (II) Dithiocarbamate Exhibits Anti-Inflammatory, Analgesic, and Antipyretic Activities through Inhibition of Inflammatory Mediators in in Vivo Models, *Naunyn-Schmiedeberg's Arch. Pharmacol.*, 2019, **392**, 961–977.

17 E. A. Afify, H. M. Alkreathy, A. S. Ali, H. A. Alfaifi and L. M. Khan, Characterization of the Antinociceptive Mechanisms of Khat Extract (Catha Edulis) in Mice, *Front. Neurol.*, 2017, **8**, 69.

18 P. Kwemo, A. Saafane, M. Vanharen, I. Durocher and D. Girard, Impact of Palladium Nanoparticles (Pd-NPs) on the Biology of Neutrophils in Vitro and on Leukocyte Attraction in Vivo, *J. Nanoparticle Res.*, 2020, **22**, 1–11.

19 B. Y. A. El-Aarag, T. Kasai, M. A. H. Zahran, N. I. Zakhary, T. Shigehiro, S. C. Sekhar, H. S. Agwa, A. Mizutani, H. Murakami and H. Kakuta, In Vitro Anti-Proliferative and Anti-Angiogenic Activities of Thalidomide Dithiocarbamate Analogs, *Int. Immunopharmacol.*, 2014, **21**, 283–292.

20 I. Hamdi, N. Mhadhbi, N. Issaoui, A. Roodt, M. M. Turnbull and H. Naïli, *J. Mol. Struct.*, 2021, **1237**, 130384.

21 I. Hamdi, N. Mhadhbi, N. Issaoui, M. El-Ghozzi, A. Tozri and H. Naïli, *J. Mol. Struct.*, 2022, **1251**, 132051.

22 *Nonius, KappaCCD Program Software*, Nonius BV, Delft, The Netherlands, 1998.

23 C. J. O'Connor, *Prog. Inorg. Chem.*, 1982, **30**, 203.

24 M. J. Frisch, G. W. Trucks, H. B. Schlegel, G. E. Scuseria, M. A. Robb, J. R. Cheeseman, G. Scalmani, V. Barone, B. Mennucci, G. A. Petersson, H. Nakatsuji, M. Caricato, X. Li, H. P. Hratchian, A. F. Izmaylov, J. Bloino, G. Zheng, J. L. Sonnenberg, M. Hada, M. Ehara, K. Toyota, R. Fukuda, J. Hasegawa, M. Ishida, T. Nakajima, Y. Honda, O. Kitao, H. Nakai, T. Vreven, J. A. Montgomery Jr, J. E. Peralta, F. Ogliaro, M. Bearpark, J. J. Heyd, E. Brothers, K. N. Kudin, V. N. Staroverov, R. Kobayashi, J. Normand, K. Raghavachari, A. Rendell, J. C. Burant, S. S. Iyengar, J. Tomasi, M. Cossi, N. Rega, J. M. Millam, M. Klene, J. E. Yazyev, J. E. Knox, J. B. Cross, V. Bakken, C. Adamo, J. Jaramillo, R. Gomperts, R. E. O. Stratmann, A. J. Austin, R. Cammi, C. Pomelli, J. W. Ochterski, R. L. Martin, K. Morokuma, V. G. Zakrzewski, G. A. Voth, P. Salvador, J. J. Dannenberg, S. Dapprich, A. D. Daniels, O. Farkas, J. B. Foresman, J. V. Ortiz, J. Cioslowski and D. J. Fox, *GAUSSIAN 09, Revision A.1*, GAUSSIAN, Inc., Wallingford CT, 2009.

25 H. B. Schlegel, Optimization of equilibrium geometries and transition structures, *J. Comput. Chem.*, 1982, **3**, 214e218.

26 National Institute of Standards and Technology (NIST). *Computational Chemistry Comparison and Benchmark Database: Precomputed Vibrational Scaling Factors*.

27 E. Runge and E. K. U. Gross, Density-functional theory for time-dependent systems, *Phys. Rev. Lett.*, 1984, **52**, 997e1000.

28 N. M. O'Boyle, A. L. Tenderholt and M. K. Langner, *J. Comput. Chem.*, 2008, **295**, 839.

29 R. Dennington, T. Keith and J. Millam, *GaussView. Journal of Semi Chemical Inorganic*, 2009, vol. 5, p. 8.

30 F. Saad, T. M. Al-Shaikh, F. Zouidi, M. A. Taher, S. A. Saidi and K. Hamden, Betalain-Enriched Beetroots Exhibit Antiulcer and Anti-Inflammatory Potentials, *J. Food Process. Preserv.*, 2023, **2023**, 9522830.

31 S. A. Saidi, T. M. Al-Shaikh and K. Hamden, Evaluation of Gastroprotective Effect of Betalain-Rich Ethanol Extract from Opuntia Stricta Var. Dillenii Employing an In Vivo Rat Model, *J. Food Qual.*, 2023, **2023**, 2215454.

32 P. P. Bradley, D. A. Priebat, R. D. Christensen and G. Rothstein, Measurement of Cutaneous Inflammation: Estimation of Neutrophil Content with an Enzyme Marker, *J. Invest. Dermatol.*, 1982, **78**, 206–209.

33 A. Buege and S. D. Aust, Microsomal Lipid Peroxidation. in *Methods in Enzymology*, Elsevier, 1978, vol. 52, pp. 302–310, ISBN 0076-6879.

34 I. D. Brown, *Acta Crystallogr.*, 1976, **A32**, 24–31.

35 K. C. Nakamoto, *Infrared and Raman Spectra of Inorganic and Coordination Compounds, Part A*, 5th edn, 1997.

36 A. Tounsi, B. Hamdi, R. Zouari and A. B. Salah, DFT (B3LYP/LanL2DZ), non-linear optical and electrical studies of a new hybrid compound: $[C_6H_{10}(NH_3)_2]CoCl_4 \cdot H_2O$, *Phys. E*, 2016, **84**, 384–394.

37 K. Azouzi, B. Hamdi, R. Zouari and A.-B. Salah, *Ionics*, 2016, **22**, 1669–1680.

38 M. A. Spackman and J. McKinnon, *CrystEngComm*, 2002, **4**, 378.

39 P. Manna, S. K. Seth, A. Das, J. Hemming, R. Prendergast, M. Helliwell, S. R. Choudhury, A. Frontera and S. Mukhopadhyay, *Inorg. Chem.*, 2012, **51**, 3557.

40 J. Sivaraman, K. Subramanian, D. Velmurugan, E. Subramanian and K. Balakrishna, Structure of vicogenin, *Acta Crystallogr., Sect. C: Cryst. Struct. Commun.*, 1993, **49**(6), 1240–1242.

41 I. B. Saad, N. Hannachi, T. Roisnel and F. Hlel, *J. Adv. Dielectr.*, 2019, **9**(5), 1950040.

42 M. Hamdi, A. Oueslati, I. Chaabane and F. Hlel, *Condens. Matter Phys.*, 2012, **750497**, 1.

43 Z.-H. Gan, N. Ni, J.-Y. Liang, C.-H. Liu, W.-X. Zheng, L. M. Yang and J.-R. Zhou, *Polyhedron*, 2018, **158**, 408.

44 J. Wang, X. Deng, F. Zhang, D. Chen and W. Ding, ZnO nanoparticle-induced oxidative stress triggers apoptosis by

activating JNK signaling pathway in cultured primary astrocytes, *Nanoscale Res. Lett.*, 2014, **9**, 117.

45 L. Merker and H. Wondratschek, *Fortschr. Mineral.*, 1957, **35**, 45–46.

46 D. G. Samsonenko, O. A. Greas'ko, T. V. Mit'kina, J. Lipkowski, A. V. Virovets, D. Fenske and V. P. Fedin, *Coord. Chem.*, 2003, **29**, 178.

47 I. B. Saad, N. Hannachi, T. Roisnel and F. Hlel, *J. Adv. Dielectr.*, 2019, **9**(5), 1950040.

48 R. Cervini, X. Li, G. Spencer, A. Holmes, S. Moratti and R. Friend, *Synth. Met.*, 1997, **84**, 359–360.

49 F. Hcini, S. Hcini, B. Alzahrani, S. Zemni and M. L. Bouazizi, *Appl. Phys. A*, 2020, **126**, 362.

50 K. W. Wagner, *Ann. Phys.*, 1913, **4**, 817.

51 K. C. Kao, *Dielectric Phenomena in Solids*, Elsevier, Amsterdam, 2004.

52 S. Singh, G. Banappanavar and D. Kabra, *ACS Mater. Lett.*, 2020, **5**, 728.

53 W. Wan, J. Luo, C. Huang, J. Yang, Y. Feng, W.-X. Yuan, Y. Ouyang, D. Chen and T. Qiu, *Ceram. Int.*, 2018, **44**, 5086–5092.

54 H. Nefzi, F. Sediri, H. Hamzaoui and N. Gharbi, *Mater. Res. Bull.*, 2013, **48**, 1978.

55 B. Louati, K. Guidara and M. Gargouri, *J. Alloys Compd.*, 2009, **472**, 347–351.

56 M. D. Migahed, N. A. Bakr, M. I. Abdel-Hamid, O. El-Hanafy and M. El-Nimr, *J. Appl. Polym. Sci.*, 1996, **59**, 655–662.

57 A. K. Pradhan, S. Saha and T. K. Nath, *Appl. Phys. A*, 2017, **123**, 715.

58 G. C. Psarras, E. Manolakaki and G. M. Tsangaris, *Composites, Part A*, 2003, **34**, 1187.

59 A. Singh, H. P. Gogoi and P. Barman, Comparative Study of Palladium (II) Complexes Bearing Tridentate ONS and NNS Schiff Base Ligands: Synthesis, Characterization, DFT Calculation, DNA Binding, Bioactivities, Catalytic Activity, and Molecular Docking, *Polyhedron*, 2022, **221**, 115895.

60 H. Kargar, V. Torabi, A. Akbari, R. Behjatmanesh-Ardakani and M. N. Tahir, Synthesis, Characterization, Crystal Structure and DFT Studies of a Palladium (II) Complex with an Asymmetric Schiff Base Ligand, *J. Mol. Struct.*, 2019, **1179**, 732–738.

61 L. Toma, G. M. Sanda, L. S. Niculescu, M. Deleanu, A. V. Sima and C. S. Stancu, Phenolic Compounds Exerting Lipid-Regulatory, Anti-Inflammatory and Epigenetic Effects as Complementary Treatments in Cardiovascular Diseases, *Biomolecules*, 2020, **10**, 641.

62 T. Behl, T. Upadhyay, S. Singh, S. Chigurupati, A. M. Alsubayiel, V. Mani, C. Vargas-De-La-Cruz, D. Uivarosan, C. Bustea and C. Sava, Polyphenols Targeting MAPK Mediated Oxidative Stress and Inflammation in Rheumatoid Arthritis, *Molecules*, 2021, **26**, 6570.